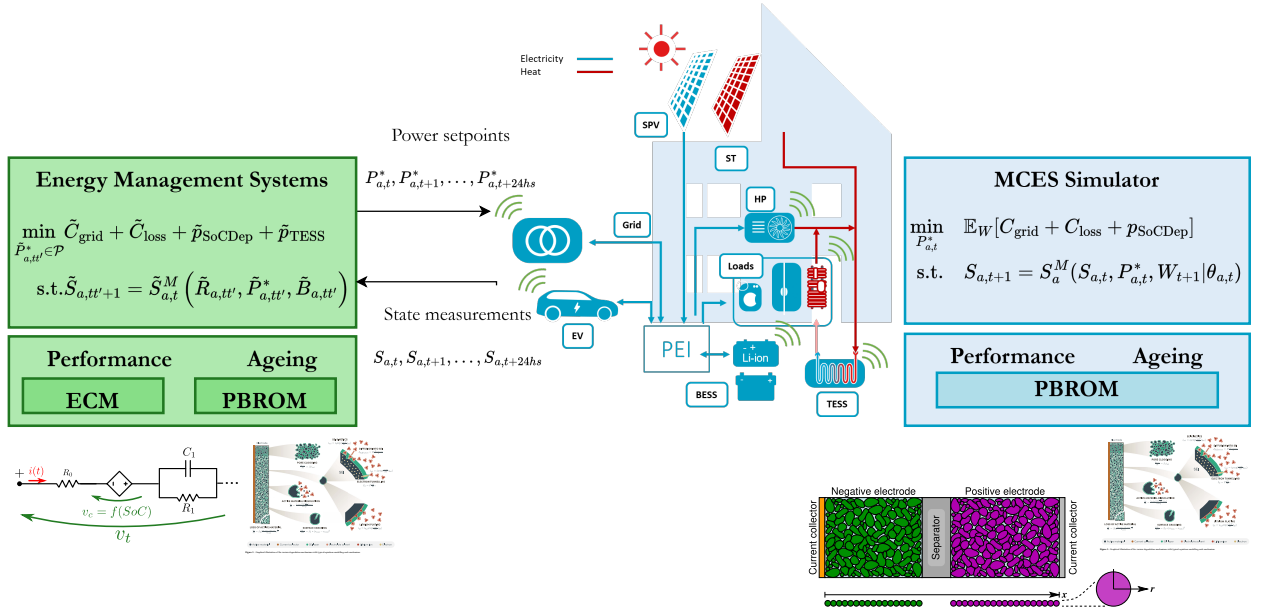


Graphical Abstract

Ageing-aware Energy Management for Residential Multi-Carrier Energy Systems

Darío Slaifstein, Gautham Ram Chandra Mouli, Laura Ramirez-Elizondo, Pavol Bauer



Highlights

Ageing-aware Energy Management for Residential Multi-Carrier Energy Systems

Darío Slaifstein, Gautham Ram Chandra Mouli, Laura Ramirez-Elizondo, Pavol Bauer

- Integrated physics-based degradation models into optimal predictive energy management for multi-carrier buildings. This allows users to trade between grid cost reductions and battery lifetime extension.
- Novel algorithm can distinguish between cathode chemistries, with LFP cells achieving lower grid costs and capacity fade than their NMC counterpart. Performance is also improved with aged batteries, while traditional benchmarks decrease their grid cost and capacity fade.

Ageing-aware Energy Management for Residential Multi-Carrier Energy Systems

Darío Slaifstein^a, Gautham Ram Chandra Mouli^a, Laura Ramirez-Elizondo^a, Pavol Bauer^a

^a*DC Systems, Energy Conversion & Storage, Electrical Sustainable Energy Department, Delft University of Technology, Mekelweg 8, Delft, 2628, Zuid-Holland, Netherlands*

Abstract

In the context of building electrification, the operation of distributed energy resources integrating multiple energy carriers (electricity, heat, mobility) poses a significant challenge due to the nonlinear device dynamics, uncertainty, and computational issues. As such, energy management systems seek to decide the power dispatch in the best way possible. The objective is to minimize and balance operative costs (energy bills or asset degradation) with user requirements (mobility, heating, etc.). Current energy management uses empirical battery ageing models outside of their specific fitting conditions, resulting in inaccuracies and poor performance. Moreover, the link to thermal systems is also overlooked. This paper presents an ageing-aware day-ahead algorithm for electrified buildings that incorporates physics-based battery ageing models. The models distinguish between energy storage systems and make explicit the trade-off between grid cost and battery degradation. The proposed day-ahead algorithm can either cut down on grid costs or extend battery lifetime (electric vehicle or stationary battery packs). Moreover, it exploits the differences between cathode chemistries improving grid costs by 25% when using LFP cells, with respect to NMC cells. Finally, the performance using aged batteries is also enhanced with 35% grid cost observed savings, when passing from new to aged batteries in the summer.

Keywords: energy management, battery degradation, multi-carrier energy system

PACS: 0000, 1111

2000 MSC: 0000, 1111

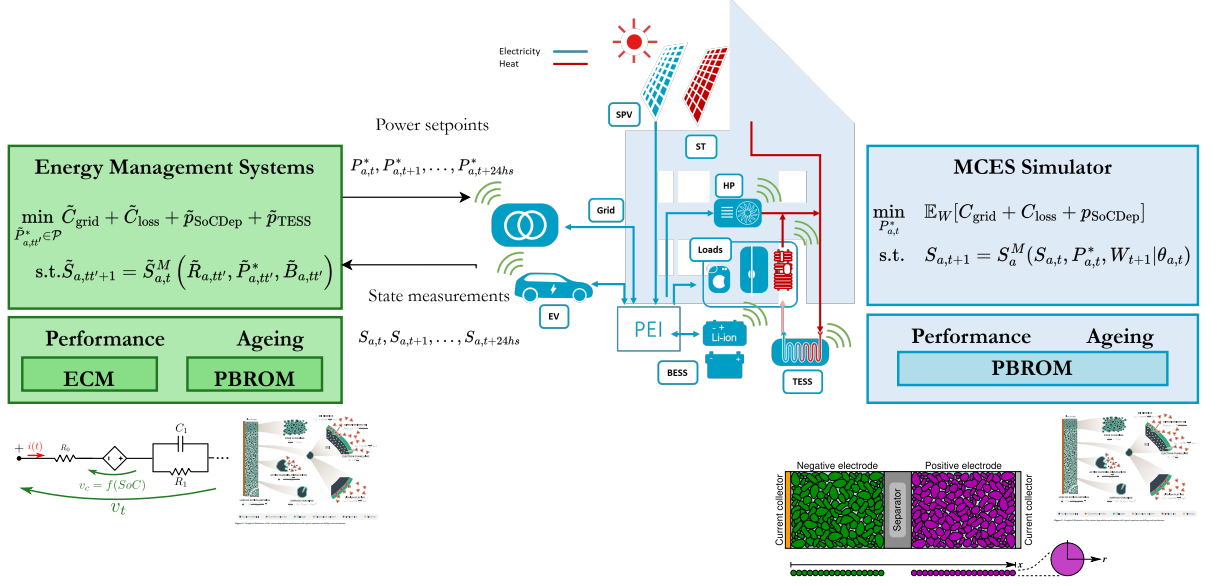


Figure 1: Schematic diagram of the proposed electrified multi-carrier building.

1. Introduction

The decarbonization of the economy as a whole is a significant challenge for modern societies. In particular, the sustainable transformation of both the energy and transport sectors poses significant technical and cultural challenges [1]. Both transitions meet/couple in the population's homes where electricity, mobility, or heat are needed. Thus, possible synergies between the three systems can be exploited to achieve the desired decarbonization, freedom, resiliency, and cost savings at the local or aggregated level [2]. The successful exploitation of such coupling thus needs to be carefully tailored and built into the design of modern multi-carrier energy systems [2–9]. This necessarily leads to advanced energy management systems (EMS) that schedule and control the distributed energy resources (DER) [6, 9–12]. Thus, the EMS needs to handle uncertainty introduced by electric vehicles [13], solar generation and loads, as well as the battery degradation [14–18]. The main goal of this work is to address this last point.

To dispatch and operate residential multicarrier energy systems (MCES), the literature suggests Model Predictive Control (MPC) [6, 12], stochastic optimization [19], reinforcement learning (RL) [6, 7, 9] and many others. Usually, the basis of such advanced systems is a day-ahead plan or dispatch

that schedules the power of the assets along the day [4, 10, 11, 20–22]. This planner is usually an optimization-based system that uses approximated deterministic forecasts of certain inputs to schedule the different assets. The decisions taken are then implemented and modified in real time. The optimization models have to model the representative aspects of the different assets of the energy system. This includes their power limits, dynamics, and operational constraints. The standard approach is to limit the models to simplified linear or quadratic forms, overlooking most technological particularities [2, 6, 9, 23–26]. In particular, when several energy storage systems are present, the EMS has to decide which storage system to use and when. In this regard, battery energy storage systems (ESS) are limited by their ageing [5, 10, 15–18, 27] as well as by their availability for mobility [5, 13]. Current battery energy storage system (BESS) control decisions impact its remaining lifetime, thus, having a control-oriented predictive model that accurately reflects the cost of current decisions is key for optimal operation [28]. The bigger the bias between the optimization model and reality the less trustworthy are the decisions and predictions made.

Unfortunately, although physical ageing mechanisms have been studied and modeled [5, 14, 29–32], they have been partially incorporated into EMS design of residential MCES through empirical ageing models [5, 10, 20, 23]. On the other hand, the interaction of electricity and heat is becoming more relevant as heating electrification intensifies, and single-carrier optimization might lead to underperformance and cost inefficiencies. In particular, electric vehicle (EV)s and heat pump (HP)s are possible sources of grid congestion [33]. When investigating MCES, Ceusters et al. [6, 7] use first-order linear models for both BESS and thermal energy storage system (TESS), neglecting any differences between their dynamics. Similarly, Ye et al. [9] does not mention any difference between storage systems nor include EVs in their system. Alpizar-Castillo, et al [34] focuses on thermal dynamics, only incorporating BESS with linear models, without including EVs. Other works only focus on the electrical carrier without including coupling electrical heating and storage [4, 10, 16, 35]. These last works apply different battery models to describe their key variables, such as state-of-charge SoC , terminal voltage v_t , and state-of-health SoH . In this multi-carrier context, the optimization needs accurate cost functions and predictive models to decide in which carrier to store energy. Since batteries are considerably expensive, optimizing operations to extend their lifetime becomes an attractive option to reduce costs.

Battery-ageing models fall within two categories: empirical or physics-based (PB) [5, 17, 27]. The first are the most widely used in the literature due to their simplicity. They are obtained by performing long standardized calendar and cycling ageing tests [5, 27]. Unfortunately, empirical degradation models only have interpolation capabilities, usually use non-linear equations, represent a limited number of operating conditions (average C-rate, minimum *SoC*, etc.), are prone to overfitting, and are chemistry dependent [32, 36]. On the other hand, PB models are built through first-principles and specialized tests to identify individual degradation mechanisms [27, 29, 31]. They have extrapolation features, can be expressed in the state-space form, account for several cathode chemistries, and represent a wide range of operating conditions. However, they are also non-linear and, in general, non-convex [27, 29–31, 37]. The integration of PB ageing models into the operation of BESS has been recently studied at the battery management system (BMS) level for standalone and EV applications [14–16, 38–40] usually through control-oriented physics-based reduced order model (PBROM). In the cited references, important cost savings were achieved either by preserving battery lifetime or by making an explicit trade-off between the grid costs and capacity fade, even when implementing optimization horizons of a day or less. To the author’s best knowledge, their integration into applications where the BESS interacts with more assets, such as transmission grids, microgrids, industry, and in particular buildings, has not been extensively researched yet [28].

In summary, current optimization-based approaches that do use PBROM to actively trade off between degradation and economic benefits are restricted to standalone battery systems [14, 15, 30, 38, 39, 41]. When the battery is integrated with larger systems (solar photovoltaics (SPV), EV, microgrid, etc.), battery dynamics are usually simplified and empirical models are used in most literature [10, 16, 35]. None of the above references include the integration with a thermal carrier or multiple storage devices, and if they do, they do not include ageing models, [24, 42]. This paper aims to bridge these three gaps.

This paper bridges the previously mentioned gaps by introducing an innovative framework that integrates **ageing physics-based reduced-order models (PBROM)** directly into the EMS planning algorithm of multi-carrier systems. Current Energy Management Systems (EMS) for residential multi-carrier energy systems (MCES) often plan day-ahead operations without a complete understanding of how their decisions impact the long-term health and lifetime of their storage assets. This integration fundamentally

changes how the EMS operates, moving from a short-sighted, one-day optimization to a more holistic, ageing-aware strategy. Our approach enables the system to choose the optimal power dispatch of each storage system based on:

- The co-optimization of both **fast electrical storage** (BESS and EV) and **slower thermal storage (TESS)**, recognizing their distinct response times and efficiencies, through distinct terminal sets.
- The recognition of different **cathode chemistries** in lithium-ion batteries, leading to different power dispatches and grid costs.
- The exploitation of parameter differences between **new and used batteries**, ensuring that the operational plan remains accurate and effective throughout the entire lifespan of the battery storage units.
- The capacity to identify **dominant degradation mechanisms**, which provides the EMS with the critical information needed to make decisions that not only meet demand but also actively preserve the health of the batteries depending on their ageing state.

2. Modeling and Optimal Planner

Our planning algorithm is an optimization-based secondary controller that minimizes energy cost and battery ageing. A schematic of the MCES and the EMS is presented in Fig. 1. The system is composed of SPV, BESS, EV, power electronic interface (PEI), HP, solar thermal (ST), TESS, grid connection and loads. On the left, the EMS decides the day-ahead schedule $P_{a,t}^*, P_{a,t+1}^*, \dots, P_{a,t+24hs}^*$, passing it down to the MCES simulator. The MCES simulator feeds back the state measurements $S_{a,t}, S_{a,t+1}, \dots, S_{a,t+24hs}$ to continue with the loop.

The following section describes the EMS models, following the Universal Modeling Framework (UMF) by Powell [43–45]. For a given system size, the objective is to handle the operation cost, which is composed of three parts: the net cost of energy from the grid C_{grid} , the degradation cost of losing storage capacity C_{loss} , and a penalty for not charging the EV p_{SoCDep} . The grid cost and the degradation cost are cumulative objectives because the goal is to optimize them through time, while the penalty for not charging the EV to the desired *SoC* level is only a point reward at departure times t_{dep} . The sequential decision problem (SPD) is then:

$$\min_{P_{a,t}^*} \mathbb{E}_W[C_{\text{grid}} + C_{\text{loss}} + p_{\text{SoCDep}}] \quad (1a)$$

$$\text{s.t. } S_{a,t+1} = S_a^M(S_{a,t}, P_{a,t}^*, W_{t+1} | \theta_{a,t}) \quad (1b)$$

$$P_{a,t}^* = X_t^\pi(S_{a,t}) \in \mathcal{P} \quad \forall a \in \mathbb{A} \quad (1c)$$

$$S_{a,t} \in \mathcal{S} \quad \forall a \in \mathbb{A} \quad (1d)$$

with

$$\mathbb{A} = \{\text{SPV, grid, EV, BESS, HP, ST, TESS}\}. \quad (2)$$

where the components of the objective are:

$$C_{\text{grid}} = w_{\text{grid}} \sum_{t=0}^T (\lambda_{\text{buy},t} \cdot P_{\text{grid},t}^+ - \lambda_{\text{sell},t} \cdot P_{\text{grid},t}^-) \cdot \Delta t \quad (3a)$$

$$C_{\text{loss}} = w_{\text{loss}} \cdot c_{\text{loss}} \cdot \sum_{t=0}^T \sum_b N_{s,b} \cdot N_{p,b} \cdot i_{\text{loss},b,t} \cdot \Delta t, \quad \forall b \in \{\text{BESS, EV}\} \subset a, \quad (3b)$$

$$p_{\text{SoCDep}} = w_{\text{SoC}} \cdot \|\varepsilon_{\text{SoC},t_{\text{dep}}}\|_2^2 \quad (3c)$$

where $S_{a,t}$ is the state vector, $P_{a,t}^*$ is the optimal decision for timestep t , W_{t+1} and is an exogenous process that introduces new information after making a decision. The mappings $S_a^M(\cdot)$, and $X_t^\pi(\cdot)$ are the transition function and optimal policy, respectively. The first is a set of equations describing the states and parameter evolution, and the second is the algorithm that finds the setpoints. The vector $\theta_{a,t}$ contains all the parameters of each asset a and changes over time t . The subindex $a \in \mathbb{A}$ corresponds to the assets shown in Fig. 1. The index b denotes the electric storage assets. The evaluation/simulation time window is T and the timestep $\Delta t = 15\text{min}$. C_{loss} is explained in Section 3.3.2 and the penalty p_{SoCDep} in Section 3.4.

The following definitions of the elements are considered:

- The actions or decision variables are

$$P_{a,t}^* = [P_{\text{EV}}, P_{\text{BESS}}, P_{\text{HP}}^e]_t^T. \quad (4)$$

- The exogenous processes/inputs to the optimization W_{t+1} are the prices λ , EV availability γ , the solar power $P_{\text{PV/ST}}$, the electric and the thermal demands $P_{\text{load}}^{e/\text{th}}$:

$$W_{t+1} = [\lambda_{\text{buy/sell}}, \gamma_{n_{\text{EV}}}, P_{\text{PV}}, P_{\text{ST}}, P_{\text{load}}^e, P_{\text{load}}^{\text{th}}]_{t+1}^T \quad (5)$$

- The state vector has 2 components, the physical state of the system R_t , and beliefs about uncertain quantities or parameters B_t . All the observable physical quantities of our system, such as currents, voltages, and so on, are included in R_t . Finally, our belief state $B_{a,t}$ is composed of forecasts of W_{t+1} . These are defined as:

$$S_{a,t} = [R_a, B_a]_t^T \quad (6a)$$

$$B_{a,t} = [\tilde{\lambda}_{\text{buy/sell}}, \tilde{\gamma}_{\text{EV}}, \tilde{P}_{\text{PV}}, \tilde{P}_{\text{ST}}, \tilde{P}_{\text{load}}^{\text{e}}, \tilde{P}_{\text{load}}^{\text{th}}]_t^T \quad (6b)$$

- The superscripts e and th refer to electricity or thermal carriers. They are used when the subscript is the same.
- Both the actions and state vectors have upper and lower limits denoted as $\overline{P}_{a,t}^*$, $\underline{P}_{a,t}^*$, $\overline{S}_{a,t}$, and $\underline{S}_{a,t}$.
- All bidirectional powers, either actions or states, are modeled with their conversion efficiency η_a :

$$\eta_a S_{a,t}^+ - \frac{1}{\eta_a} S_{a,t}^- = S_{a,t}, \quad (7)$$

with $S_t^- \perp S_t^+$

- The order of the subscript is "*name, device, time index*".
- Capital C denotes total cumulative cost in €, lowercase c denotes unit cost and lowercase w indicates tuning/scaling weight.

In Eq. 1 the planner or policy π wants to minimize the likelihood of the operational cost $\mathbb{E}[C]$ under the exogenous information process W . The problem at hand is a state-dependent problem in which our decisions $P_{a,t}^*$ are based on the current $S_{a,t}$, and influence future states $S_{a,t+1}$ (and thus, future decisions). Given the focus on future states and decisions, lookahead policies appear as attractive candidates for solving this SPD. Policy design and models are presented in the following Section 3.

3. Policy design

As mentioned before, the SPD in Eq. 1 is a state-dependent problem where current states influence future decisions. As such, Direct Lookahead

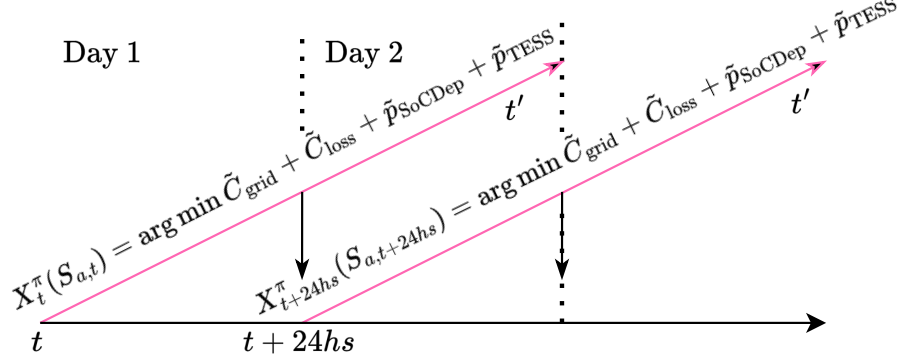


Figure 2: Deterministic DLA policy as a day-ahead planner.

(DLA) policies are commonly used in the literature to solve these problems. Two common examples of this policy family are optimal control strategies and stochastic dual dynamic programming. For this work, we focus on day-ahead planning, which is a subset of optimal control where deterministic inputs (forecast medians in this case) are used to decide the actions for the incoming day. The process is shown in Fig. 2. The scheduler takes inputs $\tilde{B}_{a,tt'}$ to decide the power dispatch $\tilde{P}_{a,tt'}^*$, optimizing over policy time $t' \in [t, t + H]$ with H the optimization horizon.

More specifically, a DLA policy based on the devices' approximated dynamic models. In this way, the EMS plans future actions based on approximate predictive models of devices. Approximation is denoted with $\tilde{\cdot}$. The policy is then solving an approximated economic optimal control problem (OCP) of the form:

$$\min_{\tilde{P}_{a,tt'}^* \in \mathcal{P}} \quad \tilde{C}_{\text{grid}} + \tilde{C}_{\text{loss}} + \tilde{p}_{\text{SoCDep}} + \tilde{p}_{\text{TESS}} \quad (8a)$$

$$\text{s.t.} \quad \tilde{S}_{a,tt'+1} = \tilde{S}_{a,t}^M \left(\tilde{R}_{a,tt'}, \tilde{P}_{a,tt'}^*, \tilde{B}_{a,tt'} \right) \quad (8b)$$

$$\tilde{S}_{a,tt'} \in \mathcal{S} \quad \forall a \in \mathbb{A} \quad (8c)$$

where

$$\tilde{p}_{\text{TESS}} = w_{\text{TESS}} \cdot \sum_{t'=t}^H \max \left(0, \tilde{S}oC_{\text{TESS},tt'} - \overline{SoC}_{\text{TESS}} \right) \Delta t \quad (9)$$

In our policy, the upper limit constraint of the TESS, $\overline{SoC}_{\text{TESS}}$, is implemented as a soft constraint to avoid infeasibilities during initialization or feedback. The penalty in the objective steers the $SoC_{\text{TESS},t}$ towards the feasible region when the weight w_{TESS} is high enough.

The deterministic optimization problem in Eq. 8 approximates the real stochastic one by using forecasts, stored in $B_{a,t}$, and approximated models for the transition function $\tilde{S}_{a,t}^M$. In this model, the time t is the time at which the DLA policy is created and t' is the time inside the policy itself. Note the subtle difference between the approximated dynamics $\tilde{S}_{a,t}^M$ and the real ones $S_{a,t}^M$. This is not to be overlooked because the assumption that the predictions made by the policy π hold true can lead to disappointing results in real-world applications. Making these distinctions early in design reveals important insights for future stages. In this work, the energy management algorithm (EMA) has an approximated model $\tilde{S}_{a,t}^M$ to decide the setpoints $\tilde{P}_{a,t'}^*$ to be implemented in a simulator $S_{a,t}^M$ containing detailed fidelity models. In the future, the simulator might as well grow enough to be considered a digital twin of the real building.

Thus the policy is:

$$X_t^\pi(S_{a,t}) = \arg \min_{P_{a,t}, \dots, P_{a,t+H}} \tilde{C}_{\text{grid}} + \tilde{C}_{\text{loss}} + \tilde{p}_{\text{SoCDep}} + \tilde{p}_{\text{TESS}} \quad (10)$$

subject to the approximate transition function $\tilde{S}_{a,t}^M$. This encompasses model approximation and forecasting ($\tilde{B}_{a,t'}$) of the future inputs (W_{t+1}). The policy is then tuned by changing the weights w and implementing different NLP solver options (warm-starting, multi-start, etc.)

A sequence matrix containing power setpoints and states from t to $t+H$ is defined as:

$$\mathcal{P}_{a,[t,t+H]} = [P_{a,t}, P_{a,t+1}, \dots, P_{a,t+H}] \quad (11)$$

$$\mathcal{S}_{a,[t,t+H]} = [S_{a,t}, S_{a,t+1}, \dots, S_{a,t+H}] \quad (12)$$

The approximate transition function $\tilde{S}_{a,t}^M(\cdot)$ is the compendium of the equations specified in the rest of this section. In the remainder of this section, all equations will be presented just in terms of t for the sake of simplicity. However, the reader must remember that when inside the policy, π they are defined under the policy's time t' .

3.1. Power & thermal balances

The thermal balance comes in as:

$$\tilde{P}_{\text{ST},t} + P_{\text{HP},t}^{\text{th}} + P_{\text{TESS},t} = \tilde{P}_{\text{load},t}^{\text{th}}. \quad (13)$$

The electric power balance, on the other hand, is:

$$\tilde{P}_{\text{PV},t} + P_{\text{BESS},t} + \gamma_{\text{EV},t} \cdot P_{\text{EV},t} + P_{\text{grid},t} = \tilde{P}_{\text{load},t}^{\text{e}} + P_{\text{HP},t}^{\text{e}}. \quad (14)$$

where γ_{EV} is the EV availability, explained in Section 3.4.

3.2. Thermal modelling

The thermal assets are modelled in a linear way:

$$P_{\text{HP},t}^{\text{th}} = \eta_{\text{HP}} \cdot P_{\text{HP},t}^{\text{e}}, \quad (15)$$

$$\tilde{P}_{\text{ST},t} = \eta_{\text{ST}} \cdot \tilde{P}_{\text{PV},t}, \quad (16)$$

and

$$SoC_{\text{TESS},t+1} = SoC_{\text{TESS},t} - \frac{\Delta t}{Q_{\text{TESS}} \cdot 3600} \cdot \eta_{\text{TESS}} \cdot P_{\text{TESS},t}, \quad (17)$$

where η denotes a conversion factor or efficiency, Q_{TESS} is the capacity in kWh. To avoid imposing an arbitrary periodicity on the TESS, no terminal conditions are used on its $SoC_{\text{TESS},t}$. Thus, the TESS operates under its natural time constant.

3.3. Batteries

The remaining devices in the MCES are all battery-based ESS. Batteries have complex nonlinear dynamics, and several modeling techniques are presented in the literature [17]. In this work, models coming from empirical and physics-based approaches are used. The modeling is divided into two different sub-models: performance and ageing. Under the UMF, this is represented in the transition function $\tilde{S}_{b,t}^M(\tilde{S}_{b,t}, x_{b,t} | \theta_{b,t})$, which contains both the perf. model $p_{b,t}^M(\cdot)$ and the ageing model $d_{b,t}^M(\cdot)$. The performance model predicts stored energy $SoC_{b,t}$ and terminal voltage $v_{t,b,t}$. The ageing model is used to update the parameters of $p_{b,t}^M(\cdot)$, as shown in Fig. 3. Even though the change in parameters $\theta_{b,t}$ becomes significant after considerable ageing has occurred, optimizing it in the short term can lead to considerable savings in the long and medium term [15, 46, 47]. This is because in PB ageing models,

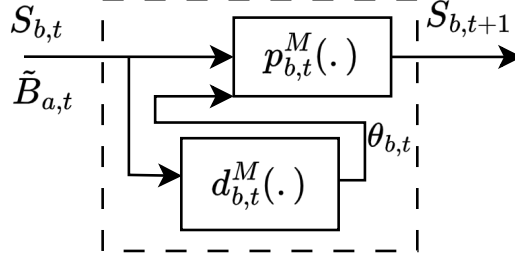


Figure 3: Storage asset transition function diagram $\tilde{S}_{b,t}^M$

the relationship between ageing states and control actions is explicit, and the policy can directly minimize it through the internal states $SoC_{b,t}$.

The perf. model is then:

$$S_{b,t+1} = p_{b,t}^M(S_{b,t}, P_{b,t}, B_{a,t} | \theta_{b,t}) \quad (18)$$

where the components of the state depend on the functional form used for the model. In general, this is a nonlinear state space system.

The ageing model $d_{b,t}^M(.)$ is a set of equations that describes the dynamics of the performance parameters $\theta_{b,t}$.

$$\theta_{b,t+1} = d_{b,t}^M(S_{b,t}, P_{b,t}, B_{a,t}, \theta_{b,t}) \quad (19)$$

Finally, a terminal constraint is implemented to ease up feasibility and mitigate symmetries in the OCP of Eq. 8, as in:

$$SoC_{\text{BESS},t'_1} = SoC_{\text{BESS},t'_1+24\text{hs}} \quad (20)$$

where $t_0 \leq t_1 \leq H \leq T$. This way, the OCP is better computationally conditioned, but the planner still has the freedom to decide $SoC_{\text{BESS},24\text{hs}}$. The proposed terminal condition has two key properties: it is more flexible than fixing $SoC_{\text{BESS},24\text{hs}} = 50\%$, and it bounds the value function V_H of the OCP. Ideally, no terminal condition would be used to freely use all 3 storage systems. Unfortunately, to solve such an unbounded OCP, an optimization horizon H much larger than 48 hours would be required [48, 49].

3.3.1. Performance models $p_{b,t}^M$

For the performance submodel, two alternatives have been implemented: a simple bucket model (BM) and a first-order equivalent circuit model (ECM).

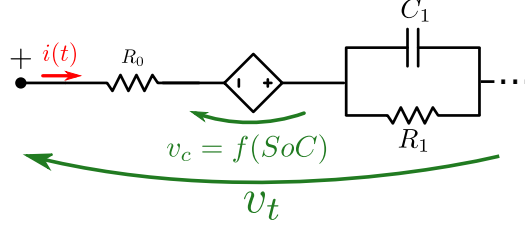


Figure 4: First-order Equivalent Circuit Model.

A basic BM of the operation of a battery assumes that its output voltage v_t is linear with the state of charge SoC , assuming no voltage drop. Hence, the only equations of this model are:

$$SoC_{b,t+1} = SoC_{b,t} - \frac{\Delta t}{Q_{b,t} \cdot 3600} \cdot \eta_c \cdot i_{b,t}, \quad (21a)$$

$$i_{b,t} = \frac{P_{b,t}}{v_{t,b,t} \cdot N_{s,b} \cdot N_{p,b}}, \quad (21b)$$

$$OCV_{b,t} = a_{OCV,b} + b_{OCV,b} \cdot SoC_{b,t}, \quad (21c)$$

$$v_{t,b,t} = OCV_{b,t}, \quad (21d)$$

$$S_{b,t} = [SoC_b, v_{t,b}, i_b]^T_t \quad (21e)$$

where $i_{b,t}$ is the current passing through the cell, $OCV_{b,t}$ is the open circuit voltage, η_c is the Coulombic efficiency [18], and $Q_{b,t}$ is the cell capacity in Ah. Each battery pack is assumed to be organized as a series connected module (SCM) where $N_{s/p, b}$ are the series cells per branch and parallel branches, respectively. In this model, the most relevant parameter in θ_b is the Q_b .

A first-order ECM has improved accuracy due to the incorporation of diffusion and series resistance, as in Fig. 4. The performance sub-model $p_{b,t}^M(\cdot)$ is then modified by adding the equation:

$$i_{R_1,b,t+1} = e^{-\frac{\Delta t}{R_{1,b} \cdot C_{1,b}}} \cdot i_{R_1,b,t} + \left(1 - e^{-\frac{\Delta t}{R_{1,b} \cdot C_{1,b}}}\right) \cdot i_{b,t} \quad (22)$$

and modifying Eq. 21d as in:

$$v_{t,b,t} = OCV_{b,t} - i_{R_1,b,t} \cdot R_{1,b} - i_{b,t} \cdot R_{0,b}, \quad (23)$$

where $i_{R_1,b,t}$ is the current flowing through R_1 in Fig. 4. Eqs. 21a, 21b and 21c are maintained. The ECM incorporates the series voltage drop that

limits power output and the first-order diffusion dynamics. Here, the relevant parameters are $\theta = [Q, R_0]^T$ that usually define the cell's state of health *SoH*.

3.3.2. Degradation models $d_{b,t}^M(.)$

For the ageing models, the first alternative is an empirical sub-model presented by [32]. The empirical sub-model reduces all the degradation mechanisms into calendar and cyclic ageing.

$$i_{\text{cycle},b,t} = \frac{c_1 \cdot c_3}{c_4} \cdot e^{c_2 \cdot |i_{b,t}|} \cdot (1 - \text{SoC}_{b,t}) \cdot |i_{b,t}|, \quad (24a)$$

$$i_{\text{cal},b,t} = c_5 \cdot e^{-\frac{24 \text{ kJ}}{RT}} \cdot \sqrt{t_{0,b} + t}, \quad (24b)$$

$$i_{\text{loss},b,t} = i_{\text{cycle},b,t} + i_{\text{cal},b,t}, \quad (24c)$$

and

$$Q_{b,t+1} = Q_{b,t} - \frac{\Delta t}{3600} \cdot i_{\text{loss},b,t}. \quad (25)$$

where the fitting parameters c_1, \dots, c_5 are taken from [10, 32, 50] and $t_{0,b}$ is the elapsed lifetime of the battery b .

For the physics-based alternative, the reduced order model (PBROM) from [15] is used. It accounts for two degradation mechanisms: the solid electrolyte interface (SEI) and active material loss (AM). The author also presents a PBROM for Li-plating, but given the low C-rate and standard temperature range of this application, it will not be included.

The growth of the SEI layer is modeled with a general reaction that aims to average all the different byproducts that compose the SEI layer. This is synthesized in the reversible SEI current i_{SEI} :

$$i_{\text{SEI},b,t} = \frac{k_{\text{SEI},b} \cdot e^{-\frac{E_{\text{SEI},b}}{RT}}}{n_{\text{SEI}} \cdot (1 + \lambda_b \cdot \beta_b) \cdot \sqrt{t_{0,b} + t}} \quad (26)$$

where $k_{\text{SEI},b}$ is the kinetic rate of the average reaction, $E_{\text{SEI},b}$ is the activation energy of the reaction, n_{SEI} is the average number of e^- transferred through the layer, and λ_b and β_b are parameters depending on other variables such as $\eta_{k,b}$, $OCV_{n,b}$, z_b and others.

The system is completed with:

$$\eta_{k,b,t} = \frac{2 \cdot R \cdot T}{F} \cdot \sinh^{-1} \left(\frac{i_{b,t}}{n_{\text{SEI}} \cdot a_s \cdot A \cdot L_n \cdot i_0} \right) \quad (27a)$$

$$z_{b,t} = \text{SoC}_{b,t} \cdot (z_{100\%,b} - z_{0\%}) + z_{0\%,b} \quad (27b)$$

$$\beta_b = e^{\frac{n_{\text{SEI}} \cdot F}{R \cdot T} \cdot (\eta_{k,b} + OCV_{n,b,t} - OCV_{s,b})} \quad (27c)$$

where η_k is the SEI side reaction kinetic overpotential, z is the Li stoichiometry of the cell, OCV_n is the open-circuit voltage of the anode made with an empirical fit, $OCV_s = 0.4V$ is the side reaction open-circuit voltage, and T is the cell temperature. It is assumed that the temperature T is constant over time and is controlled by the local primary control system. For the BESS this assumption could be challenged given that the BESS is owned/operated by the same house owners. In the case of the EV, the ownership of the car battery pack sometimes corresponds to the OEM/car manufacturer, limiting access and control over it. The rest of the parameters can be found in the Appendix A.

The loss of active material due to the mechanical stress of the electrode is modeled with:

$$i_{AM,b,t} = k_{AM,b} \cdot e^{\frac{-E_{AM,b}}{R \cdot T}} \cdot SoC_{b,t} \cdot |i_{b,t}| \cdot Q_{b,0} \quad (28)$$

The total ageing is the contribution of both mechanisms SEI layer growth and AM loss. The capacity fade current is:

$$i_{loss,b,t} = i_{SEI,b,t} + i_{AM,b,t} \quad (29)$$

which is later used again in 25.

Now, by carefully inspecting Eq. 23, the reader will notice that if $R_{0,b,t}$ is incorporated as a variable in the OCP, Eq. 8, this would add another non-convex constraint to it (since $i_{b,t}$ can be either positive or negative). Thus, its evolution is only included in the simulator $S_{a,t}^M(.)$ updating the parameters without the policy X_t^π being directly aware of the process.

To model the power fade (i.e., the increase of R_0), the SEI layer thickness $\delta_{SEI,b,t}$ growth is described by:

$$\delta_{SEI,b,t+1} = \delta_{SEI,b,t} + \frac{\Delta t}{M_{SEI} \cdot n_{SEI} \cdot F \cdot \rho_{SEI} \cdot A_n} i_{SEI,b,t} \quad (30)$$

Hence, the dynamics of the series resistance R_0 are:

$$R_{0,b,t+1} = R_{0,b,t} + \frac{\varepsilon_s}{\kappa_{eff}} \cdot \frac{\Delta t}{M_{SEI} \cdot n_{SEI} \cdot F \cdot \rho_{SEI} \cdot A_n} i_{SEI,b,t} \quad (31)$$

The solvent S leaves the electrolyte to form the SEI layer; thus, the volume fraction of S evolves with:

$$\varepsilon_{e,b,t+1} = \varepsilon_{e,b,t} - a_s \cdot \frac{\Delta t}{M_{SEI} \cdot n_{SEI} \cdot F \cdot \rho_{SEI} \cdot A_n} i_{SEI, b, t} \quad (32)$$

3.4. Electric Vehicle

From the point of view of a residential building, the EVs are a BESS with availability constraints and certain requirements regarding their *SoC* at departure time t_{dep} . For the availability γ , the probability distributions of departure (t_{dep}) and arrival (t_{arr}) times can be described as random variables $t_{\text{dep/arr}} \sim \mathcal{T}_{\text{dep/arr}}$, whose distributions $\mathcal{T}_{\text{dep/arr}}$ are taken from Elaad [51]. The availability γ_t will then be:

$$\gamma_t = \begin{cases} 0 & t \in [t_{\text{dep}}; t_{\text{arr}}] \\ 1 & \text{otherwise} \end{cases}. \quad (33)$$

The power balance of an EV is

$$P_{\text{tot,EV},t} = \gamma_{\text{EV},t} P_{\text{EV},t} + (1 - \gamma_{\text{EV},t}) P_{\text{drive,EV}} \quad (34)$$

where $P_{\text{tot,EV},t}$ is the total power of the EV, $P_{\text{EV},t}$ is the charger power, and $P_{\text{drive,EV}}$ is the power consumed driving, assuming no public charging. The total power $P_{\text{tot,EV},t}$ is then used in Eq. (21b) and later for calculating the ageing of the EV batteries. The average driving power is also sampled from a Gaussian distribution $P_{\text{drive,EV}} \sim \mathcal{N}(\mu_{\text{drive}}, \sigma_{\text{drive}}^2)$. This is because the EV battery pack degradation during driving needs to be accounted for in the operation strategy (charging and driving).

At t_{dep} the EV is required to be delivered at SoC_{dep}^* :

$$SoC_{\text{EV}}(t_{\text{dep}}) = SoC_{\text{dep}}^* \quad (35)$$

This is implemented as a penalty in the objective function, Eq. 8, as in any typical OCP. The deviation from the reference at the desired time is penalized with:

$$\varepsilon_{\text{SoC},t_{\text{dep}}} = SoC_{\text{EV}}(t_{\text{dep}}) - SoC_{\text{dep}}^* \quad (36)$$

Summing up, the three different storage systems have three different ways of handling their terminal set and value function bounds. The BESS has a periodic condition in Eq. 20, which is a flexible alternative to the classic terminal daily periodicity. The EV follows a soft-tracking problem at t_{dep} . The TESS has no terminal condition. This flexible design is the key contribution to integrating all the storage systems and the non-convex PB models to OCP in Eq. 8.

Algorithm 1 MCES simulation

- 1: **Define setpoint sequences** $\mathcal{P}_{a,[t,t+24\text{hs}]}$
 - 2: **Define exogenous information sequences** $\mathcal{W}_{[t+1,t+1+24\text{hs}]}$
 - 3: Recalculate $P_{\text{TESS},t}$ and $P_{\text{grid},t}$ with Eqs. 13, 14, $\mathcal{P}_{a,[t,t+24\text{hs}]}$, and $\mathcal{W}_{a,[t+1,t+1+24\text{hs}]}$
 - 4: **for** $t \in \mathcal{D}_t$ **do**
 - 5: Simulate $SoC_{\text{TESS},t}$ using Eq. 17
 - 6: Simulate b performance using $p_b^M(\cdot)$ PBROM [52]
 - 7: Simulate b degradation using $d_{b,t}^M(\cdot)$ PBROM [15]
 - 8: **end for**
 - 9: Feed-back $\mathcal{S}_{a,[t,t+(H+\Delta t)/2]}$ to the planner
-

4. MCES Simulator $S_{a,t}^M(\cdot)$

The simulator evaluates the policy π and closes the loop with the state measurements. It is designed to:

- Provide high-accuracy simulation results that act as plant measurements.
- Adjust/reject setpoints that violate hard constraints.
- Re-balance power in case of rejections or infeasible optimizations.

The whole process is defined in Algorithm 1. First, the power setpoints must be adjusted for the grid and TESS because the forecast used in X_t^π will never be the same as the actual exogenous inputs. Take a look at the balances, Eq. 13 and 14, which contain the loads and solar generation. It is clear that $\tilde{P} \neq P$ and a device must compensate for that difference. Thus, the simulator $S_{a,t}^M$ recalculates:

$$P_{\text{TESS},t} = P_{\text{load},t}^{\text{th}} - P_{\text{ST},t} - P_{\text{HP},t}^{\text{th}}. \quad (37)$$

$$P_{\text{grid},t} = P_{\text{load},t}^{\text{e}} + P_{\text{HP},t}^{\text{e}} - P_{\text{PV},t} - P_{\text{BESS},t} - \gamma_{\text{EV},t} \cdot P_{\text{EV},t}. \quad (38)$$

Second, once these powers have been adjusted, the simulator uses these powers to obtain the true/actual/fidelity state sequence $\mathcal{S}_{a,[t,t+(H+\Delta t)/2]}$. For the TESS it recalculates Eq. 17. For the b , it uses LiBRA.jl [52] to swiftly simulate PBROMs of the performance of the battery [17, 53]. After that, the

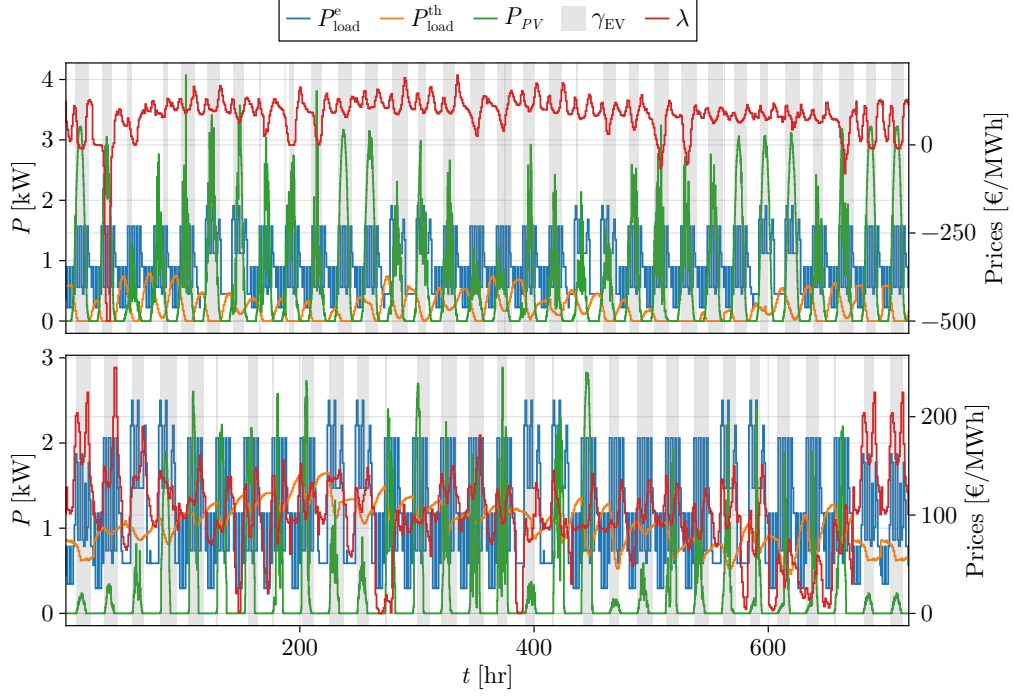


Figure 5: Exogenous information W_{t+1} . Grey bands represent periods where the EV is not connected.

models from Jin [15] are used to calculate the true degradation outcome of the decisions $P_{a,t}^*$. Again, the reader must remember that the capacity fade (decrease in $Q_{b,t}$) is modeled in both the simulator $S_{a,t}^M$ and the approximate model of the planner $\tilde{S}_{a,t}^M$, whereas the power fade (increase in $R_{0,as,t}$) is only addressed in the simulator $S_{a,t}^M$. Finally, if an action $P_{b,t}^*$ causes a future state to go out of bounds ($S_{b,t+1} \leq \underline{S}_b$ or $S_{b,t+1} \geq \overline{S}_b$), the remaining actions are rejected and the b remains in that state (either \overline{S}_b or \underline{S}_b) until the next day. Finally, the carriers are rebalanced if necessary.

The final state sequence $\mathcal{S}_{a,[t,t+(H+\Delta t)/2]}$ is then fed back to the optimization-based planner. For practical implementation, in which the simulator is, in fact, an experimental setup, an online state observer is necessary to feed back the states to the EMS. This is particularly important for the ESS [17, 18, 54].

Algorithm 2 Rolling horizon algorithm

- 1: **Initialize hyperparameters** $t_0, \Delta t, t_W, w, n_d$
 - 2: **Initialize device states and inputs** $S_{a,0}$
 - 3: **for** $d \in 1 : n_d$ **do**
 - 4: Solve the deterministic OCP, Eq. 8, and obtain $P_{a,t}^*$.
 - 5: Simulate $S_{a,t+1} = S_{a,t}^M(S_{a,t}, P_{a,t}^*, W_{t+1}) \forall t \in \mathcal{D}_t = [t; t + 24\text{hs}]$, using Algorithm 1
 - 6: Update forecasts in $\tilde{B}_{a,t}$
 - 7: Move time window $\mathcal{D}_t^\pi \leftarrow \mathcal{D}_t^\pi + 24\text{hs}$;
 - 8: **end for**
-

5. Case studies

The building has a grid connection with a smart meter with 15min resolution. The grid power P_{grid} is included in the state vector $S_{a,t}$.

The system is composed of a 5kWp SPV, a 20kWh BESS with nickel manganese cobalt oxides (NMC) or Lithium iron phosphate (LFP) cells, two 12.5kW EV charging points, a 4kW_e heat pump, a 2.7kW_{th} solar thermal collector, a 200kWh TESS, a 6kWp electrical load, a 1kWp thermal demand, and 10kW LV grid connection. Power consumption profiles (P_{load}^e) were constructed for a year using data from 2021 to 2023 from TU Delft's Green Village smart meter data [55]. The output of the SPV is taken from [56, 57], the market prices λ are taken from the EPEX day-ahead auction, and $\lambda_{\text{buy}} = 0.95\lambda_{\text{sell}}$ [58], and the heat demand $P_{\text{load}}^{\text{th}}$ was modeled as [34].

The cells used are SANYO NCR18650 cells for NMC as in [15] and A123 cells for LFP [31]. Their datasets were taken from PyBaMM [59] and LiBRA [52]. The ECMs for both cell types were fitted from synthetic cells simulated in PyBaMM, following the methodology in [17]. Once the simulated profiles are ready, the ECM parameters can be identified using subspace system identification as in [60]. The parameters can be found in Appendix A, Tables A.4 and A.5. The capacity fade cost is assumed to be $c_{\text{loss}} = 1.2$ €/Ah, roughly 280-310€/kWh, depending on the average voltage.

The OCP and simulations were modelled and run using Julia [61], JuMP [62], and InfiniteOpt [63]. The chosen solver was KNITRO's active sets algorithm from Artelys since it can handle NLP with complementarity constraints [64]. All simulations were run using an Intel CPU at 2.60GHz and 4 processors and 32GB of RAM.

5.1. Case Study I: Day-ahead planning

To test and validate our EMA the planner was simulated for two standard months (summer and winter) using 2023 data from the previously mentioned sources. Both are presented in Fig. 5. To quantify the impact of each performance and ageing model 3 day-ahead planners, 2 benchmarks and our proposed approach, were implemented:

- (*BNoDeg*) Including a bucket model and no degradation $w_{\text{loss}} = 0$, with $\tilde{S}_{a,t}^{M1}$ in Eq. 8.
- (*CEmpDeg*) Including a first-order ECM and empirical ageing for the b , with $\tilde{S}_{a,t}^{M2}$ in Eq. 8.
- (*CPBDeg*) Including first-order ECM with PBROM ageing for the b , with $\tilde{S}_{a,t}^{M3}$ in Eq. 8.

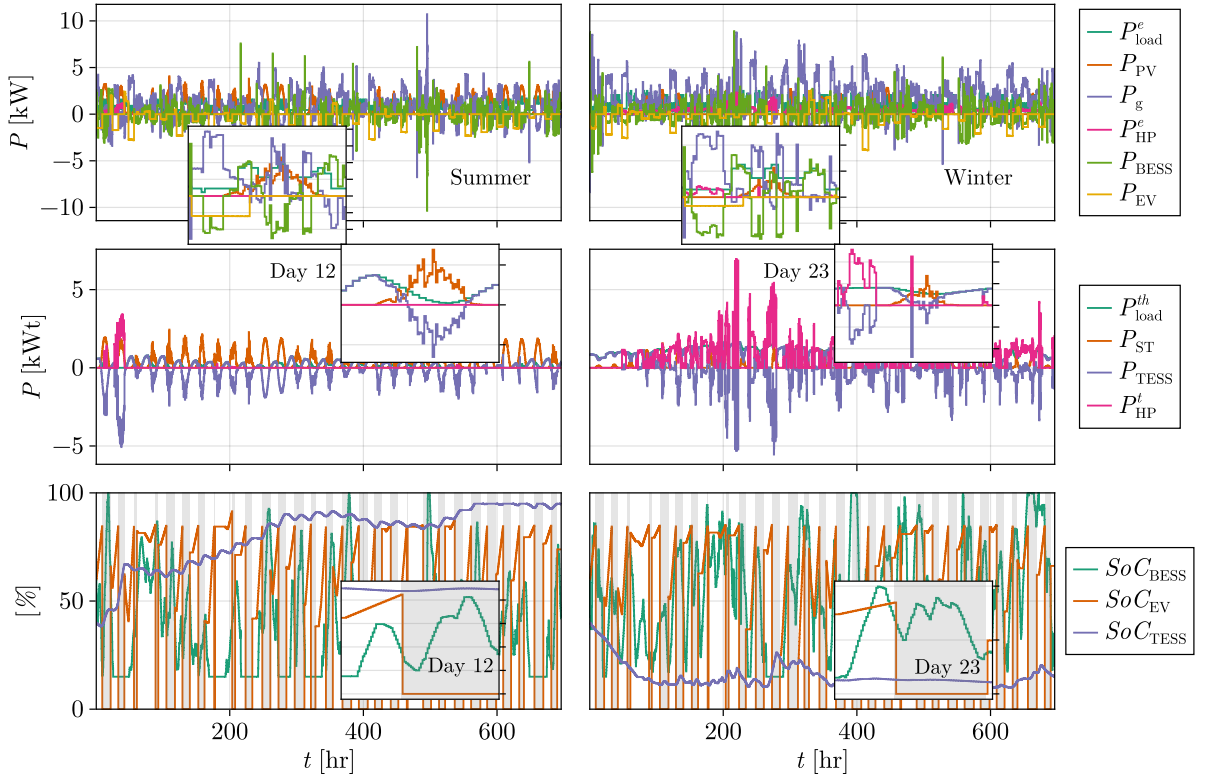


Figure 6: Monthly dispatch of MCES under CPBDeg-DA planner for summer (left) and winter (right).

The simulation workflow is presented in Algorithm 2 and depicted in Fig. 2. First, the hyperparameters are initialized. This includes the time window to be optimized $\mathcal{D}_t^\pi = [t; t + H]$, the number of days n_d , user preferences, the initial state $S_{a,0}$, and weights w . In our case for day-ahead planning, the time window is $H = 48\text{hr} - \Delta t$ and $n_d = 29$. The weights are $w_{\text{grid}} = w_{\text{loss}} = 1$ and $w_{\text{SoCDep}} = w_{\text{TESS}} = 1000$, since the first two represent real economic costs and the second represent penalties. At timestep t , the OCP in Eq. 8, is solved, obtaining the action sequence $\mathcal{P}_{a,[t,t+24\text{hs}]}^*$. Together with the exogenous information sequence $\mathcal{W}_{[t+1,t+24\text{hs}]}$ the actions are passed to the simulator $S_{a,t}^M$ to get the feedback state sequence $\mathcal{S}_{a,[t,t+24\text{hs}]}$. This feedback loop is repeated n_d times.

As a representative example, Fig. 6 presents the results for the proposed *CPBDeg* planner for a monthly period. It has the resulting power balances (electrical and thermal) and the use of the hybrid energy storage system (HESS). The electric ESS have daily cycles to minimize operating costs (energy arbitrage). This is particularly important for the EV since its mobility demand already establishes a daily periodicity. Thus, due to the EV's battery pack size and its natural periodicity, it becomes the main electric storage of the system. This frees up the BESS for energy arbitrage, trying to capture price variations when possible within the power balance. Thus, price volatility incentivizes cycling. However, due to the SEI model, batteries are also pushed downwards to the minimum ageing state at $\underline{\text{SoC}}_{b,t}$. Hence, the dispatch contemplates a trade-off between the 2 parts of the objective C_{grid} and Q_{loss} . On the thermal carrier, the $P_{\text{load},t}^{\text{th}}$ represents the heat losses of the building which have to be compensated by either ST, HP or TESS. In the summer, the losses during solar hours are almost zero and thus the ST charges the TESS. If the prices are negative enough then HP charges the TESS during $\lambda_t \leq 0$. In the winter, the TESS is charged with the HP early in the day when prices are low or during solar hours, in that order of priority, to later deliver heat to the demand at high price hours. In summary, during the summer price volatility is high with several hours with $\lambda_t \leq 0$, the EMS buys this energy to reduce costs. In winter, prices are less volatile and the load is higher, leading to fewer opportunities for arbitrage and overall higher costs.

The schedules of the HESS under the different planners are summarized in Figs. 7- 9. In the BESS, Fig. 7, the *BNoDeg* and *CEmpDeg* cycle the battery pack more often. This is because *BNoDeg* does not contemplate ageing, and the *CEmpDeg* equations do not relate $\min Q_{\text{loss}}$ to $\underline{\text{SoC}}$. The *CPBDeg*

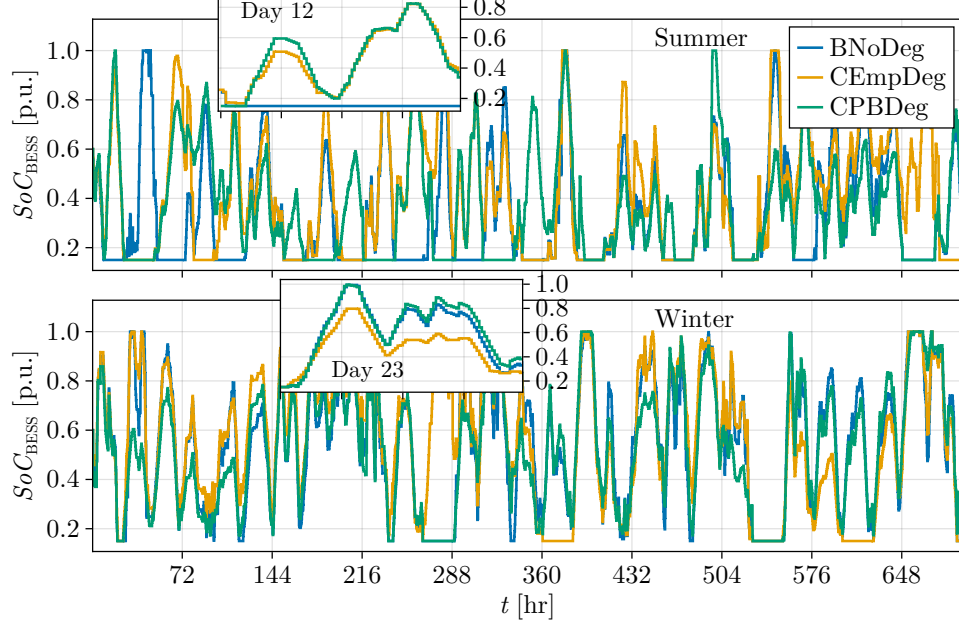


Figure 7: Monthly simulation SoC_{BESS} for summer (top) and winter (bottom).

planner cycles less frequently, concentrating the operation near $P = 0$ and \underline{SoC} to reduce the ageing of the BESS. This is true for both summer (top) and winter (bottom). Moreover, on many days the price variations are not large enough to afford ageing the BESS, thus $CPBDeg$ chooses to maintain the SoC below the benchmarks. The two highlighted days are days where the $CPBDeg$ outperforms the benchmarks and the BESS prioritizes C_{grid} over Q_{loss} . Finally the linear $BNoDeg$ is the planner with the highest percentage of rejects, roughly 45% of the total time in the summer. This is because when the $BNoDeg$ plans for high-power discharges its predicted $\tilde{SoC}_{b,t}$ deviates from the true $SoC_{b,t}$ of the simulator $S_{a,t}^M$, wrongly depleting the ESS early (lower bound $\underline{SoC}_{b,t}$).

For the EV timeseries comparison, Fig.8, the user's mobility requirement leads to similar timeseries for all the planners. In general, $CPBDeg$ delays the charging to extend the V2G as much as possible, to avoid \overline{SoC}_{EV} . V2G mode is less frequent in the $BNoDeg/CEmpDeg$ than in the $CPBDeg$ because of this, and is valid in both standard seasons. This counterintuitive result is because the ageing PBROM show how Q_{loss} is minimized by \underline{SoC} . Since p_{SoCDep} requires high SoC_{dep}^* , this results in more V2G.

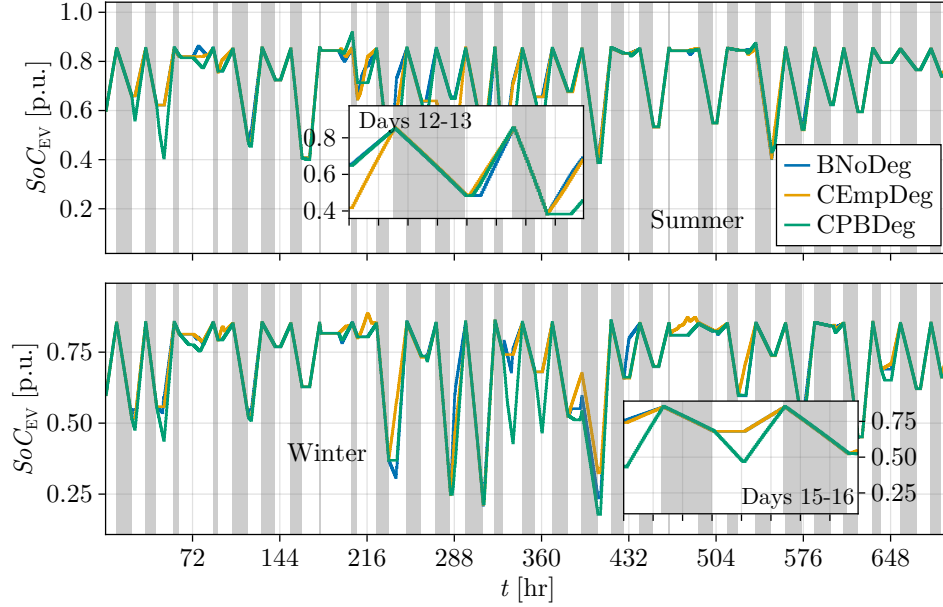


Figure 8: Monthly simulation SoC_{EV} for summer (top) and winter (bottom). Grey bands indicate driving periods.

On the thermal side, presented in Fig. 9, the natural periodicity of the carrier is longer due to its thermal efficiencies and size. Hence, during the first week the initial $SoC_{TESS,0}$ influences costs greatly. After the first week, the EMS has already steered the buffer to its desired setpoint. This means a high $SoC_{TESS,t}$ during summer (high heat generation, low load) and a low setpoint during winter (low heat generation, high load). The high setpoint during summer entails 2 risks: overcharging the TESS (i.e., activating soft-constraint and curtailing ST) and not capturing negative prices prices due to past short-sightedness (TESS starting a day with a high SoC). Even though in the summer $CPBDeg$ has the smallest ST curtailment the ageing models have a low overall impact. In other words, integrating ageing models does not change the overall TESS decisions.

In summary, each storage system follows a distinct use represented in its terminal set. The EV follows a soft-tracking penalty $p_{SoC_{Dep}}$, the BESS follows a flexible daily periodicity, and the TESS handles medium-term thermal demand. Without the design of the mixed terminal set, the non-convex NLP would not converge to feasible locally optimal points, and thus is a key

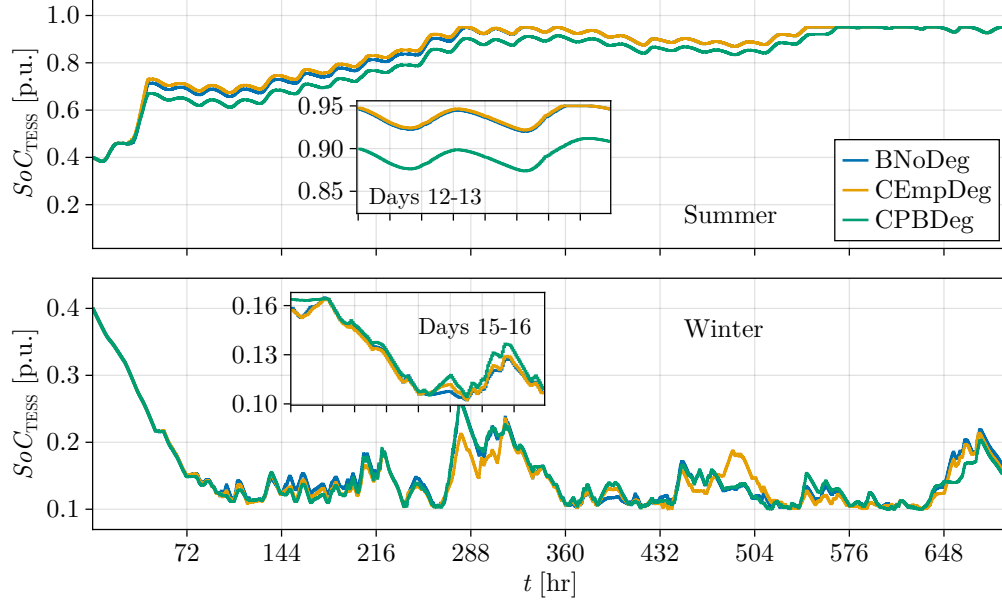


Figure 9: Monthly simulation SoC_{TESS} for summer (top) and winter (bottom).

Planner	C_g [€]		Q_{loss} [mAh]	
	summer	winter	summer	winter
BNoDeg	16.01	77.33	206.9	249.2
CEmpDeg	15.22	77.45	216.4	236.7
CPBDeg	20.28	78.25	206.6	234.3

Table 1: Planner comparison cost summary.

contribution of this paper.

The performance of each planner is summarized in Table 1. Starting with the grid cost C_{grid} , the best performer is the *CEmpDeg* in the summer and *BNoDeg* in the winter. The differences between the first and second are less than 1 €. The worst performer is *CPBDeg*. For the total capacity fade Q_{loss} , *CEmpDeg* has the highest degradation in the summer and *BNoDeg* has the highest in the winter. The proposed ageing-aware *CPBDeg* achieves the lowest degradation in both seasons, maintaining a reasonable C_{grid} .

In general, the planner that has the lowest C_{grid} is the one with the highest Q_{loss} , but this is not always *BNoDeg*. The *CEmpDeg* fails to minimize the total capacity fade because of its model bias ($S_{a,t}^M \neq \hat{S}_{a,t}^M$), in which it is

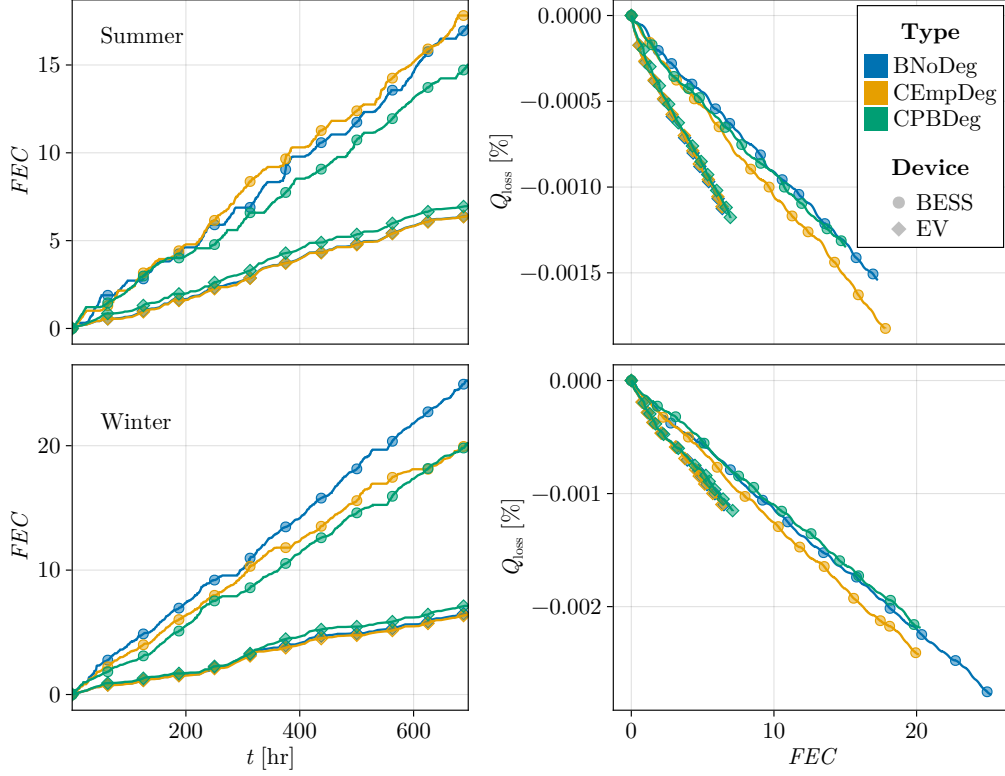


Figure 10: Full equivalent cycles FEC over time (left) and relative capacity fade Q_{loss} over FEC (right).

rewarded to cycle at \overline{SoC}_b and a calendar ageing independent of the $SoC_{b,t}$. Additionally, the linear *BNoDeg* planner fails to fulfill its predictions because of the high number of rejected actions during summer.

To dive deeper into the total storage usage, a quantitative analysis of the number of cycles done by the b is necessary. Figure 10 presents the full equivalent cycles FEC over time t , showing that the *CPBDeg* planners increase the EV usage FEC_{EV} at the expense of doing fewer cycles with the BESS. When analyzing the capacity fade Q_{loss} against the full eq. cycles FEC , Fig. 10, it is clear that the relative degradation per cycle ($\frac{\partial Q_{\text{loss}}}{\partial FEC}$) of the *CPBDeg* is smaller in the winter than the used benchmarks. In summer, the *BNoDeg* has the lowest degradation per cycle due to its high number of rejects. The use of the EVs is the same for all planners, because the trajectory is mostly driven by user mobility. Finally, in both seasons, *CEmpDeg* presents the

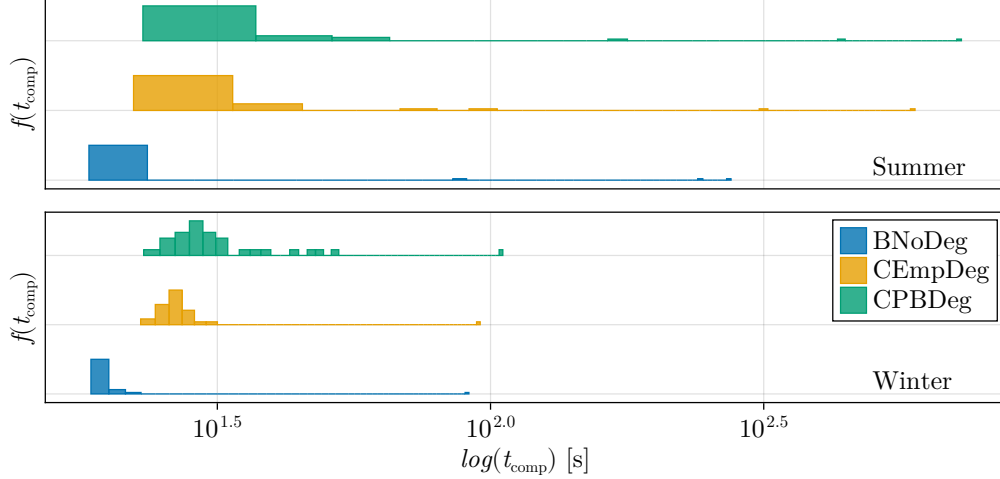


Figure 11: Distributions of computational time t_{comp} .

highest $\frac{\partial Q_{\text{loss}}}{\partial FEC}$. This appears to be a risky strategy due to a lack of consistency across seasons and objectives (minimizing degradation or minimizing grid costs). Lastly, even though the capacity fade is not significant in $T = 1$ month, daily optimization can have a significant impact in the long term, as it was shown in [39, 46, 47]. As a final note, if the C-rate is increased (≥ 1) and battery temperature T is not constant, the degradation on a daily basis can be significantly higher.

Finally, the computational time for the different strategies is presented in Fig. 11. Each sample is the total computational time it takes to solve Algorithm 2. Unexpectedly, *BNoDeg* has the lowest and most consistent t_{comp} distribution, i.e., the smallest standard deviation. However, both *CEmpDeg* and *CPBDeg* planners have similar empirical distributions, maintaining overall fast computational time. Hence, the increase in modeling accuracy of PBROM is not prohibitively expensive when compared to its empirical counterpart. This is to be expected as the empirical ageing model is also non-linear and non-convex. In summary, this case study shows that:

- *CPBDeg* achieves the smallest $\frac{\partial Q_{\text{loss}}}{\partial FEC}$ (best ageing control) and smallest total Q_{loss} .
- The computational cost of *CPBDeg* is not prohibitive when compared to its empirical benchmark *CEmpDeg*.

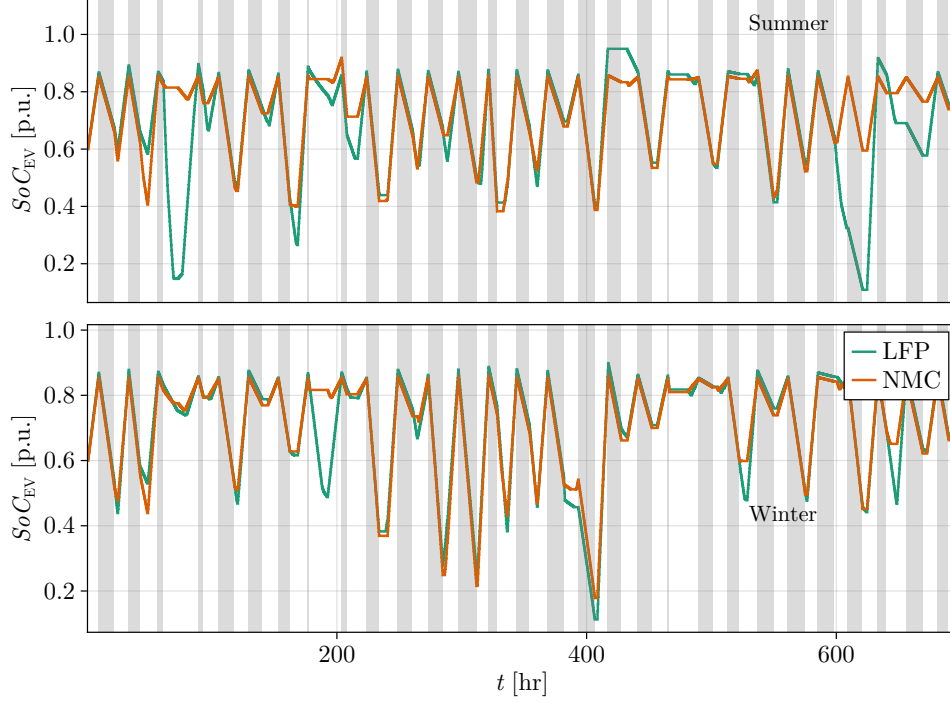


Figure 12: Cathode comparison simulation SoC_{EV} . Grey bands indicate driving periods.

- *BNoDeg* achieves one of the smallest C_{grid} with fast computational times, as expected.

5.2. Case Study II: Managing different cathodes

To demonstrate the PB models' flexibility and extended capabilities, the *CPBDeg* scheduler is tested using two similar battery packs of the same rated capacity Q but using different cells. One is formed with NMC cells and the other with LFP. Since LFP cells have a lower rated capacity of $Q_n = 2.3$ Ah and a lower *OCV*, the battery packs have more $N_{s/p}$ to have roughly the same pack-rated capacity as their NMC counterparts. The power limits $\bar{P}_{b,t}$, $\underline{P}_{b,t}$ are also maintained to make an even comparison.

The PB ageing models are suitable for both because they have graphite anodes [15, 30]. Nevertheless, they have different electrolytes. This is addressed by changing the electrolyte parameters in the model. The same model equations are used, but with different parameter values. This is a great advantage compared to the empirical fits presented in the literature.

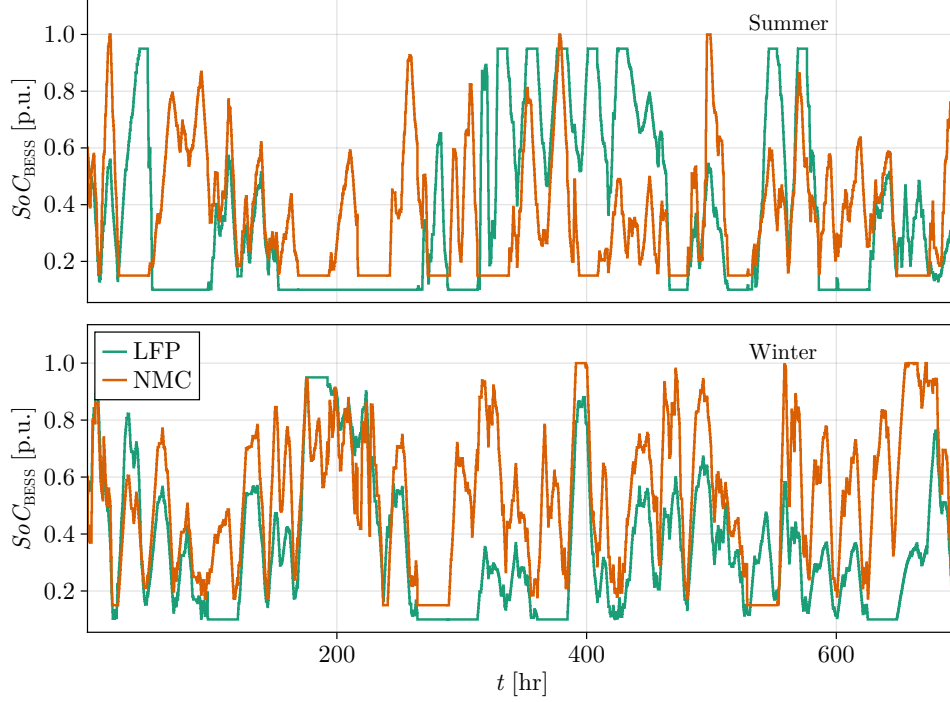


Figure 13: Cathode comparison simulation SoC_{BESS} .

In the latter, the derived models are prone to overfitting to training conditions, delivering complex non-linear equations that can only be applied to specific chemistries and operating conditions.

The simulation results are presented in Figs. 12 - 14. Starting with the EV, Fig. 12, the operation is similar except for a few days in summer and winter in which the LFP decides to have deeper discharges than its NMC counterpart. Moving forward to the BESS, Fig. 13, in summer, the LFP scheduler is too ambitious, generating early storage depletion roughly 40% of the time, 10% more than the NMC cells. During the winter, total rejections are reduced to 25% and 10% for LFP and NMC, respectively.

Continuing with the ageing analysis Fig. 14 presents the FEC and Q_{loss} results. When looking at the EV, the FEC_{EV} increases with the LFP cells. The opposite happens to the BESS, which reduces its cycles in the LFP pack. In combination with its lower calendar ageing, represented in the parameter set, the LFP packs achieve lower degradation per eq. cycle $\frac{\partial Q_{loss}}{\partial FEC}$

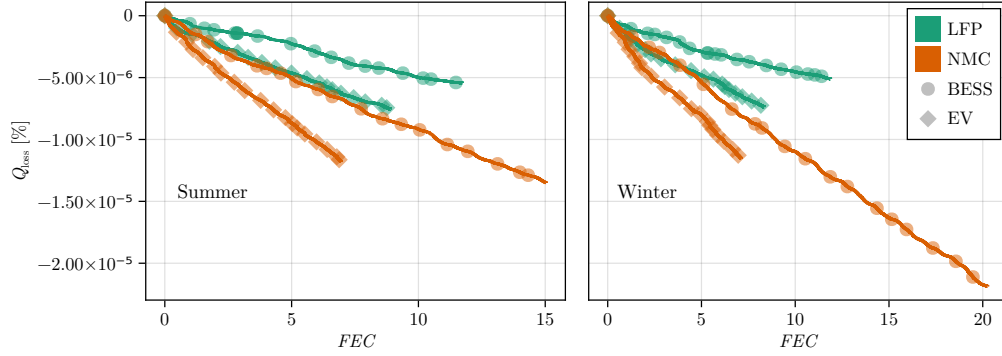


Figure 14: Case Study 2 - LFP and NMC cells degradation analysis.

Cell cathode	C_g [€]		Q_{loss} [mAh]	
	summer	winter	summer	winter
LFP	15.25	78.36	152.1	147.1
NMC	20.28	78.25	206.6	234.3

Table 2: Cathode comparison cost summary.

than their NMC counterpart. As such, the *CPBDeg-LFP* reduces BESS total throughput (FEC) and capacity fade Q_{loss} while increasing EV throughput and reducing its degradation.

Table 2 presents the summary of performance for both cell types. Overall, the *CPBDeg-LFP* achieves lower total costs and ageing despite its high number of rejected actions. During winter C_{grid} stays the same with 37% less degradation. However, in the summer, just by changing the cell type from NMC to LFP C_{grid} is reduced by 25%, similar to *BNoDeg* in Section 5.1, and roughly 25% less capacity fade. This shows that *CPBDeg* rightly exploits its physical information of the system to achieve better performance.

5.3. Case Study III: Managing aged and fresh batteries

To demonstrate the flexibility and extended capabilities of the *CPBDeg* planner the scheduler is tested using two battery packs: the first is the fresh battery pack of NMC cells of Section 5.1 and the second is the same pack but with cells aged at $SoH = 90\%$. Only one benchmark is used: a *BNoDeg* with no SoH update. Thus, the *BNoDeg* EMS sees a perfectly healthy cell with rated capacity when in reality the battery pack is aged 10%. There is

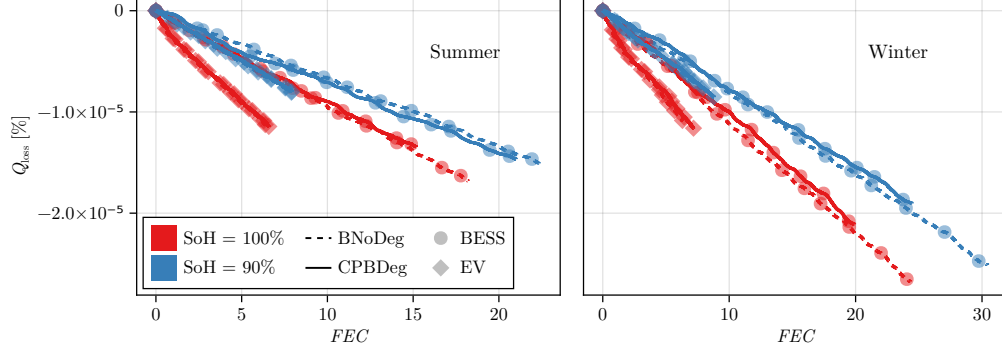


Figure 15: Case Study 3 - new and aged cells degradation analysis.

no empirical benchmark because the only parameter that can be update in it is the initial lifetime $t_{0,b}$, only affecting calendar ageing. The update is based on a 5% increase in series resistance $R_{b,0}$ and 10% decrease of the available Li content $z_{100\%,b}$ and its propagation with the equations of Section 3.3.2.

Figure 15 presents the degradation patterns for the 2 planners and different SoH . In the aged battery, the share of calendar ageing (against the total) within $i_{SEI,b,t}$ is much smaller and thus the percentual Q_{loss} is almost 35% smaller than in the new battery packs. In both seasons, the EVs patterns are similar for both *BNoDeg* and *CPBDeg*. The change in EV trajectories between aged and fresh cells shows a slight increase FEC , due to a smaller rated capacity, and a decrease in relative ageing, due to reduced calendar ageing. The impact on the BESS is more pronounced. In winter, *CPBDeg* has a smaller $\frac{\partial Q_{loss}}{\partial FEC}$ (upper-right hand side of the graph) for both aged and new cells, with *BNoDeg* doing more eq. cycles. In the winter *CPBDeg* still has a smaller $\frac{\partial Q_{loss}}{\partial FEC}$ in the new cell but not in the used cell, where this is achieved by the benchmark controller. In other words, as the battery ages, the predominance of calendar ageing within the SEI layer is diminished. Thus, the link between $i_{b,t}$ and $Q_{loss,b,t}$ becomes stronger, due to the predominance of active material loss and the cyclic component of the SEI layer.

For the current simulation time T of 1 month and average C-rate below 1C, the degradation slope may appear linear to the naked eye. However, in Fig. 15, the trajectory of the aged battery is also presented, and its average slope is smaller than the new battery degradation slope ($\frac{\Delta Q_{loss,b}}{\Delta FEC_b} |_{SoH=90\%} < \frac{\Delta Q_{loss,b}}{\Delta FEC_b} |_{SoH=100\%}$). This is due to the nonlinear dependency of $i_{SEI,b,t}$ with

Planner	C_g [€]		Q_{loss} [mAh]	
	summer	winter	summer	winter
SoH 100 %				
CPBDeg	24.7	79.0	202.0	232.8
BNoDeg	14.9	76.9	212.0	243.6
SoH 90 %				
CPBDeg	16.3	78.7	130.0	149.0
BNoDeg	15.2	77.6	132.3	158.3

Table 3: Cost and degradation summary.

\sqrt{t} . Thus, it is clear that even though each trajectory might appear linear, over longer simulation times of several months and years, the dependency is non-linear.

Finally, when adding the costs to the analysis, summarized in Table 3, it is noticed that *CPBDeg* achieves lower capacity fade Q_{loss} than *BNoDeg* across all seasons and *SoH*. Even improving the total grid cost C_{grid} as the cells degrade. In particular during summer, with a 35% observed improvement. On the other hand, *BNoDeg* worsens its performance as the cells degrade with higher C_{grid} , Q_{loss} and model bias.

In summary, the performance of the proposed *CPBDeg* planner comparatively improves when using used cells, with respect to its linear *BNoDeg* benchmark. This is because the ageing PBROMs encapsulate the fade of calendar ageing (\sqrt{t}) and rise of cyclic SEI and AM ($i_{b,t}$, $SoC_{b,t}$) as the battery ages.

5.4. Limitations & Future works

- This paper assumes that battery pack temperatures are constant (BESS and EV), since temperature control is part of the local primary controls performed by the respective BMS. Future research could explore active thermal controls and their impact on degradation control.
- Even though the terminal set is more flexible than the standard literature, the design is still arbitrary. It would be interesting to design the terminal conditions as part of a wider control scheme, such as seasonal optimization.
- Forecasts are needed for all exogenous processes W_{t+1} .

- State observers are also necessary for all devices in an experimental application to correctly feed back the states $S_{a,t}$ to the optimization.
- The thermal flow-based models used in this paper assume a fixed building temperature decided in an external system. This is the assumption behind $P_{\text{load}}^{\text{th}}$. Flexible thermal controls could also be integrated.
- Uncertainty handling is limited since re-optimization frequency is only 24 hours. Future works include improving this through dynamic programming approaches and/or economic model predictive control.

6. Conclusions & Discussion

In summary, this paper presents an optimization-based day-ahead planner for residential multi-carrier energy systems that uses PBROM models to integrate battery ageing. Its integration with the thermal and mobility carriers is achieved by designing specific terminal sets for the individual storage systems, depending on their use and technology. The proposed *CPBDeg* planner can handle different cathode chemistries as well as batteries in different ageing states. The planner does this with lower degradation than the benchmarks. The PBROM integration comes at the expense of slightly higher computational times and grid cost in the case of NMC cells.

In the first case study, it is shown how advanced PBROM can be used to reduce battery ageing while maintaining a grid cost comparable to benchmarks, in accordance with the literature for standalone utility-scale applications [27, 38, 39, 41, 65]. This is because the planner can better control the degradation per full equivalent cycle than the benchmarks.

In the second case study, the proposed planner is equipped with battery packs of different cathode chemistries, and its performance is compared. Empirical models are cathode-specific and thus can't handle multiple cell chemistries. The LFP battery pack has a lower total Q_{loss} as per established knowledge and can achieve lower grid costs C_{grid} than its NMC counterpart. Even more so, when considering that the relative cost c_{loss} for both packs was the same, when in reality LFP packs have a lower cost than NMC packs. Thus, Section 5.2 is a conservative approximation, and LFP packs have the potential to enable even lower operation costs. The grid savings are achieved just by changing some simple model parameters taken from the literature. This flexibility is an essential feature because it allows the EMS to exploit any battery pack at hand fully.

The last case study showed how the proposed EMA handles aged and new batteries seamlessly, even improving performance as the battery ages, improving the summer grid cost by 35%. The reason is that the EMA can identify predominant degradation mechanisms from the ageing PBROM, exploiting the decrease of SEI importance over time and the rise of active material loss. Its linear counterpart, however, is unaware of the degradation, increasing the number of rejected actions. Summing up, grid costs can be reduced by using LFP battery packs or modifying objective weights, the latter at the expense of higher degradation. Finally, the integration of ageing PBROMs has a low impact on the HP and TESS, meaning that the almost 25% of grid cost savings of Section 5.2 are achieved without fundamentally modifying the thermal strategy. In applications where scalability and fast computation are key drivers, decomposition strategies could be explored to exploit this coupling.

7. Acknowledgment

The project was carried out with a Top Sector Energy subsidy from the Ministry of Economic Affairs and Climate, carried out by the Netherlands Enterprise Agency (RVO). The specific subsidy for this project concerns the MOOI subsidy round 2020, FLEXINet project grant number MOOI 32027.

8. Declaration of generative AI and AI-assisted technologies in the writing process

During the preparation of this work, the author(s) used ChatGPT and Gemini to help the writing process in favor of clarity and readability. After using this tool/service, the author(s) reviewed and edited the content as needed and take(s) full responsibility for the content of the published article.

Appendix A. Appendix: A

Graphite anode open-circuit voltage:

$$\begin{aligned}
OCV_{n,b,t}(z_{b,t}) = & 0.6379 + 0.5416 \cdot e^{-305.5309 \cdot z_{b,t}} \\
& + 0.044 \cdot \tanh\left(-\frac{z_{b,t} - 0.1958}{0.108}\right) \\
& - 0.1978 \cdot \tanh\left(\frac{z_{b,t} - 1.0571}{0.0854}\right) \\
& - 0.6875 \cdot \tanh\left(\frac{z_{b,t} + 0.0117}{0.0529}\right) \\
& - 0.0175 \cdot \tanh\left(\frac{z_{b,t} - 0.5692}{0.0875}\right)
\end{aligned} \tag{A.1}$$

Table A.4 presents the model parameters for the PBROMs.

Parameter	Description	Units	NMC (SANYO cell)	LFP (A123 cell)
n_{SEI}	Number of e^- transferred in SEI side reaction	-		2.0
λ	Constant $\lambda = \frac{c_s \sqrt{D_s}}{c_p \sqrt{D_p}}$	-		5.51×10^{-5}
OCV_s	OCV of the side reaction	V		0.4
ε_{AM}	Active material volume fraction	-		0.552
R_s	Particle radius	m	7.5×10^{-6}	5×10^{-6}
a_s	Specific surface area of the anode	m^{-1}		$\frac{3 \cdot \varepsilon_{AM}}{R_s}$
A_n	Active surface area of the anode	m^2	0.105	0.18
L_n	Thickness of anode	m	50×10^{-6}	34×10^{-6}
i_0	Exchange current of the intercalation current	A/ m^2		1.5
k_{SEI}	Kinetic rate	$1/\sqrt{s}$		66.85
E_{SEI}	Activation energy	J/mol		39146.0
$\delta_{SEI,0}$	Initial value of the SEI layer thickness	m		2.0×10^{-9}
M_{SEI}	Molecular weight of the SEI layer	kg/mol		0.162
ρ_{SEI}	Density of the SEI layer	kg/ m^3		1690.0
$z_{100\%}$	Full electrode stoichiometry	-	0.9	0.81
$z_{0\%}$	Empty electrode stoichiometry	-	0	0.0176
k_{AM}	Kinetic rate	1/Ah		0.0137
E_{AM}	Activation energy	J/mol		39500.0
β	Tuning parameter	-		1.7
t_0^+	Transport/transference number	-	0.363	0.36
E_κ	Activation energy for κ	J/mol		34700.0
E_{D_e}	Activation energy for D_e	J/mol		34700.0
κ_{ref}	Reference ionic conductivity for κ at reference temperature	S/m		0.174
$D_{e,ref}$	Reference value for D_e at reference temperature	m^2/s		7.5×10^{-11}
$brug$	Bruggeman coefficient	-		3/2
$c_{e,avg}$	Average volume concentration of Li in the electrolyte	mol/ m^3	1000	1200
$c_{e,max}$	Maximum volume concentration of Li in the electrolyte	mol/ m^3	1000	1200
σ_n	Electronic conductivity	S/m	100	215
ε_s	Volume fraction of solid electrolyte	-	0.59	0.58

Table A.4: Parameter values, descriptions, and units for PBROMs.

For the first-order ECMs the model parameters are presented in Table A.5.

Parameter	Unit	NMC (SANYO cell)	LFP (A123 cell)
η_c	%	99.5	99.9
Q_0	Ah/cell	5.29	2.29
R_0	$m\Omega$	28.11	27.01
$\tau_1 = R_1 C_1$	s	2.35	2.13
R_1	$m\Omega$	33.57	26.98

Table A.5: Parameter values, descriptions, and units for ECMs.

References

- [1] IEA, Net Zero by 2050: A Roadmap for the Global Energy Sector, International Energy Agency (2021) 224.
- [2] M. Geidl, G. Andersson, Optimal Power Flow of Multiple Energy Carriers, IEEE Transactions on Power Systems 22 (1) (2007) 145–155. doi:10.1109/TPWRS.2006.888988. URL <https://ieeexplore.ieee.org/document/4077107/>
- [3] G. Andersson, E. Zurich, M. Geidl, Optimal power dispatch and conversion in systems with multiple energy carriers PlanGridEV View project BPES-Optimal sizing and control of balancing power in the future EU power system considering transmission constraints View project OPTIMAL POWER DISPATCH, Proceedings 15th Power Systems Computation Conference (PSCC). (2005). URL <https://www.researchgate.net/publication/228776936>
- [4] W. Vermeer, G. R. C. Mouli, P. Bauer, Real-Time Building Smart Charging System Based on PV Forecast and Li-Ion Battery Degradation, Energies 2020, Vol. 13, Page 3415 13 (13) (2020) 3415. doi:10.3390/EN13133415. URL <https://www.mdpi.com/1996-1073/13/13/3415/html><https://www.mdpi.com/1996-1073/13/13/3415>
- [5] W. Vermeer, G. R. Chandra Mouli, P. Bauer, A Comprehensive Review on the Characteristics and Modeling of Lithium-Ion Battery Aging, IEEE Transactions on Transportation Electrification 8 (2) (2022) 2205–2232. doi:10.1109/TTE.2021.3138357. URL <https://ieeexplore.ieee.org/document/9662298/>

- [6] G. Ceusters, R. C. Rodríguez, A. B. García, R. Franke, G. Deconinck, L. Helsen, A. Nowé, M. Messagie, L. R. Camargo, Model-predictive control and reinforcement learning in multi-energy system case studies, *Applied Energy* 303 (2021) 117634. doi:10.1016/j.apenergy.2021.117634.
URL <https://linkinghub.elsevier.com/retrieve/pii/S0306261921010011>
- [7] G. Ceusters, L. R. Camargo, R. Franke, A. Nowé, M. Messagie, Safe reinforcement learning for multi-energy management systems with known constraint functions, *Energy and AI* 12 (2023) 100227. doi:10.1016/j.egyai.2022.100227.
URL <https://doi.org/10.1016/j.egyai.2022.100227><https://linkinghub.elsevier.com/retrieve/pii/S2666546822000738>
- [8] D. Van Der Meer, G. R. C. Mouli, G. M. E. Mouli, L. R. Elizondo, P. Bauer, Energy Management System with PV Power Forecast to Optimally Charge EVs at the Workplace, *IEEE Transactions on Industrial Informatics* 14 (1) (2018) 311–320. doi:10.1109/TII.2016.2634624.
- [9] Y. Ye, D. Qiu, X. Wu, G. Strbac, J. Ward, Model-Free Real-Time Autonomous Control for a Residential Multi-Energy System Using Deep Reinforcement Learning, *IEEE Transactions on Smart Grid* 11 (4) (2020) 3068–3082. doi:10.1109/TSG.2020.2976771.
URL <https://ieeexplore.ieee.org/document/9016168/>
- [10] W. Vermeer, G. R. C. Mouli, P. Bauer, Optimal Sizing and Control of a PV-EV-BES Charging System Including Primary Frequency Control and Component Degradation, *IEEE Open Journal of the Industrial Electronics Society* 3 (2022) 236–251. doi:10.1109/OJIES.2022.3161091.
URL <https://ieeexplore.ieee.org/document/9740621/>
- [11] W. Vermeer, G. R. Chandra Mouli, P. Bauer, A Multi-Objective Design Approach for PV-Battery Assisted Fast Charging Stations Based on Real Data, 2022 IEEE Transportation Electrification Conference and Expo, ITEC 2022 (2022) 114–118doi:10.1109/ITEC53557.2022.9814016.
- [12] A. Esmaeel Nezhad, A. Rahimnejad, P. H. J. Nardelli, S. A. Gadsden, S. Sahoo, F. Ghanavati, A Shrinking Horizon Model Predictive

- Controller for Daily Scheduling of Home Energy Management Systems, *IEEE Access* 10 (2022) 29716–29730. doi:10.1109/ACCESS.2022.3158346.
URL <https://ieeexplore.ieee.org/document/9732346/>
- [13] P. Alexeenko, E. Bitar, Achieving reliable coordination of residential plug-in electric vehicle charging: A pilot study, *Transportation Research Part D: Transport and Environment* 118 (2023) 103658. doi:10.1016/j.trd.2023.103658.
URL <https://linkinghub.elsevier.com/retrieve/pii/S136192092300055X>
- [14] M. A. Xavier, A. K. de Souza, K. Karami, G. L. Plett, M. S. Trimboli, A Computational Framework for Lithium Ion Cell-Level Model Predictive Control Using a Physics-Based Reduced-Order Model, *IEEE Control Systems Letters* 5 (4) (2021) 1387–1392. doi:10.1109/LCSYS.2020.3038131.
URL <https://www.ieee.org/publications/rights/index.htmlhttps://ieeexplore.ieee.org/document/9259035/>
- [15] X. Jin, Aging-Aware optimal charging strategy for lithium-ion batteries: Considering aging status and electro-thermal-aging dynamics, *Electrochimica Acta* 407 (2022) 139651. doi:10.1016/j.electacta.2021.139651.
URL <https://linkinghub.elsevier.com/retrieve/pii/S0013468621019356>
- [16] Y. Li, Y. Yang, J. Tang, B. Xiong, X. Deng, D. Tang, Design of Degradation-Conscious Optimal Dispatch Strategy for Home Energy Management System With Rooftop PV and Lithium-Ion Batteries, in: 2019 4th International Conference on Intelligent Green Building and Smart Grid (IGBSG), IEEE, 2019, pp. 741–746. doi:10.1109/IGBSG.2019.8886194.
URL <https://ieeexplore.ieee.org/document/8886194/>
- [17] G. L. Plett, *Battery Management Systems Volume I Battery Modeling*, Artech House Power Engineering and Power Electronics, 2015.
URL <https://us.artechhouse.com/Battery-Management-Systems-Volume-1-Battery-Mo.aspx>

- [18] G. L. Plett, BATTERY MANAGEMENT SYSTEMS Volume II: Equivalent-Circuit Methods, first edit Edition, Artech House Power Engineering and Power Electronics, 2016.
URL <https://us.artechhouse.com/Battery-Management-Systems-Volume-II-Equivalent.aspx>
- [19] Z. Chen, L. Wu, Y. Fu, Z. Chen, L. Wu, Real-Time Price-Based Demand Response Management for Residential Appliances via Stochastic Optimization and Robust Optimization, IEEE Transactions on Smart Grid 3 (2012). doi:10.1109/TSG.2012.2212729.
- [20] M. J. Risbeck, Mixed-Integer Model Predictive Control with Applications to Building Energy Systems (2018).
- [21] T. Jouini, A. Bensmann, T. Lilge, R. Hanke-Rauschenbach, M. Müller, Predictive Operation of Multi-Energy Systems in Sequential Markets: A Case Study, in: 2024 European Control Conference (ECC), IEEE, 2024, pp. 1509–1515. doi:10.23919/ECC64448.2024.10591115.
URL <https://ieeexplore.ieee.org/document/10591115/>
- [22] P. Li, T. Guo, M. Abeysekera, J. Wu, Z. Han, Z. Wang, Y. Yin, F. Zhou, Intraday multi-objective hierarchical coordinated operation of a multi-energy system, Energy 228 (2021) 120528. doi:10.1016/j.energy.2021.120528.
URL <https://linkinghub.elsevier.com/retrieve/pii/S0360544221007775>
- [23] D. Mariano-Hernández, L. Hernández-Callejo, A. Zorita-Lamadrid, O. Duque-Pérez, F. Santos García, A review of strategies for building energy management system: Model predictive control, demand side management, optimization, and fault detect & diagnosis, Journal of Building Engineering 33 (2021) 101692. doi:10.1016/J.JOBE.2020.101692.
- [24] S. Yang, H. O. Gao, F. You, Building electrification and carbon emissions: Integrated energy management considering the dynamics of the electricity mix and pricing, Advances in Applied Energy 10 (2023) 100141. doi:10.1016/J.ADAPEN.2023.100141.
URL <https://www-sciencedirect-com.tudelft.idm.oclc.org/science/article/pii/S2666792423000203#fig0001>

- [25] M. Mittelviefhaus, G. Georges, K. Boulouchos, Electrification of multi-energy hubs under limited electricity supply: De-/centralized investment and operation for cost-effective greenhouse gas mitigation, *Advances in Applied Energy* 5 (2022) 100083. doi:10.1016/J.ADAPEN.2022.100083.
URL <https://www.sciencedirect.com/science/article/pii/S2666792422000014>
- [26] Q. Su, Z. Gao, Z. Zhong, Dynamic energy hub-based planning and operation for optimal integration of variable energy conversion efficiency in community-level energy systems, *Energy* 332 (2025) 137143. doi:10.1016/J.ENERGY.2025.137143.
URL <https://www.sciencedirect.com/science/article/pii/S0360544225027859#sec4>
- [27] J. M. Reniers, G. Mulder, D. A. Howey, Review and Performance Comparison of Mechanical-Chemical Degradation Models for Lithium-Ion Batteries, *Journal of The Electrochemical Society* 166 (14) (2019) A3189–A3200. doi:10.1149/2.0281914jes.
URL <https://iopscience.iop.org/article/10.1149/2.0281914jes>
- [28] V. Vega–Garita, M. Heydarzadeh, A. H. Dadash, E. Immonen, The need for aging-aware control methods in lithium-ion batteries: A review, *Journal of Energy Storage* 132 (2025) 117653. doi:10.1016/J.EST.2025.117653.
URL <https://www.sciencedirect.com/science/article/pii/S2352152X25023667?via%3Dihub>
- [29] S. E. J. O’Kane, W. Ai, G. Madabattula, D. Alonso-Alvarez, R. Timms, V. Sulzer, J. S. Edge, B. Wu, G. J. Offer, M. Marinescu, Lithium-ion battery degradation: how to model it, *Physical Chemistry Chemical Physics* 24 (13) (2022) 7909–7922. doi:10.1039/D2CP00417H.
URL <http://xlink.rsc.org/?DOI=D2CP00417H>
- [30] X. Jin, A. Vora, V. Hoshing, T. Saha, G. Shaver, R. E. García, O. Wasynczuk, S. Varigonda, Physically-based reduced-order capacity loss model for graphite anodes in Li-ion battery cells, *Journal of Power Sources* 342 (2017) 750–761. doi:10.1016/j.jpowsour.2016.12.099.

URL <https://linkinghub.elsevier.com/retrieve/pii/S037877531631802X>

- [31] E. Prada, D. Di Domenico, Y. Creff, J. Bernard, V. Sauvant-Moynot, F. Huet, A Simplified Electrochemical and Thermal Aging Model of LiFePO₄-Graphite Li-ion Batteries: Power and Capacity Fade Simulations, *Journal of The Electrochemical Society* 160 (4) (2013) A616–A628. doi:10.1149/2.053304JES/XML.
URL <https://iopscience.iop.org/article/10.1149/2.053304jes>
<https://iopscience.iop.org/article/10.1149/2.053304jes/meta>
- [32] J. Wang, J. Purewal, P. Liu, J. Hicks-Garner, S. Soukazian, E. Sherman, A. Sorenson, L. Vu, H. Tataria, M. W. Verbrugge, Degradation of lithium ion batteries employing graphite negatives and nickel-cobalt-manganese oxide + spinel manganese oxide positives: Part 1, aging mechanisms and life estimation, *Journal of Power Sources* 269 (2014) 937–948. doi:10.1016/j.jpowsour.2014.07.030.
URL <https://linkinghub.elsevier.com/retrieve/pii/S037877531401074X>
- [33] N. Damianakis, G. R. C. Mouli, P. Bauer, Y. Yu, Assessing the grid impact of Electric Vehicles, Heat Pumps & PV generation in Dutch LV distribution grids, *Applied Energy* 352 (2023) 121878. doi:10.1016/J.APENERGY.2023.121878.
- [34] J. Alpízar-Castillo, L. M. Ramírez-Elizondo, P. Bauer, Modelling and evaluating different multi-carrier energy system configurations for a Dutch house, *Applied Energy* 364 (2024) 123197. doi:10.1016/j.apenergy.2024.123197.
URL <https://linkinghub.elsevier.com/retrieve/pii/S0306261924005804>
- [35] Y. Li, D. M. Vilathgamuwa, D. E. Quevedo, C. F. Lee, C. Zou, Ensemble Nonlinear Model Predictive Control for Residential Solar Battery Energy Management, *IEEE Transactions on Control Systems Technology* 31 (5) (2023) 2188–2200. doi:10.1109/TCST.2023.3291540.
URL <https://ieeexplore.ieee.org/document/10186024/>

- [36] J. Schmalstieg, S. Käbitz, M. Ecker, D. U. Sauer, A holistic aging model for Li(NiMnCo)O₂ based 18650 lithium-ion batteries, *Journal of Power Sources* 257 (2014) 325–334. doi:10.1016/j.jpowsour.2014.02.012.
URL <https://linkinghub.elsevier.com/retrieve/pii/S0378775314001876>
- [37] J. Purewal, J. Wang, J. Graetz, S. Soukiazian, H. Tataria, M. W. Verbrugge, Degradation of lithium ion batteries employing graphite negatives and nickel–cobalt–manganese oxide + spinel manganese oxide positives: Part 2, chemical–mechanical degradation model, *Journal of Power Sources* 272 (2014) 1154–1161. doi:10.1016/J.JPOWSOUR.2014.07.028.
- [38] J. M. Reniers, D. A. Howey, Digital twin of a MWh-scale grid battery system for efficiency and degradation analysis, *Applied Energy* 336 (2023) 120774. doi:10.1016/J.APENERGY.2023.120774.
URL <https://linkinghub.elsevier.com/retrieve/pii/S0306261923001381>
- [39] J. M. Reniers, G. Mulder, D. A. Howey, Unlocking extra value from grid batteries using advanced models, *Journal of Power Sources* 487 (December 2020) (2021) 229355. doi:10.1016/j.jpowsour.2020.229355.
URL <https://doi.org/10.1016/j.jpowsour.2020.229355><https://linkinghub.elsevier.com/retrieve/pii/S0378775320316438>
- [40] Y. Li, T. Wik, Y. Huang, C. Zou, Nonlinear Model Inversion-Based Output Tracking Control for Battery Fast Charging, *IEEE Transactions on Control Systems Technology* 32 (1) (2024) 225–240. doi:10.1109/TCST.2023.3306240.
- [41] J. M. Reniers, G. Mulder, S. Ober-Blöbaum, D. A. Howey, Improving optimal control of grid-connected lithium-ion batteries through more accurate battery and degradation modelling, *Journal of Power Sources* 379 (September 2017) (2018) 91–102. doi:10.1016/j.jpowsour.2018.01.004.
URL <https://doi.org/10.1016/j.jpowsour.2018.01.004><https://linkinghub.elsevier.com/retrieve/pii/S0378775318300041>
- [42] J. Marqusee, W. Becker, S. Ericson, Resilience and economics of microgrids with PV, battery storage, and networked diesel

- generators, *Advances in Applied Energy* 3 (2021) 100049. doi:10.1016/J.ADAPEN.2021.100049.
URL <https://www-sciencedirect-com.tudelft.idm.oclc.org/science/article/pii/S266679242100041X>
- [43] W. B. Powell, A unified framework for stochastic optimization, *European Journal of Operational Research* 275 (3) (2019) 795–821. doi:10.1016/J.EJOR.2018.07.014.
- [44] W. B. Powell, *Sequential Decision Analytics and Modeling Modeling with Python, Now Foundations and Trends*, 2022.
- [45] W. Powell, *Reinforcement Learning and Stochastic Optimization: A Unified Framework for Sequential Decisions*, Vol. 22, Wiley, 2022. doi:10.1080/14697688.2022.2135456.
URL <https://www.tandfonline.com/doi/full/10.1080/14697688.2022.2135456>
- [46] Y. Cao, S. B. Lee, V. R. Subramanian, V. M. Zavala, Multiscale model predictive control of battery systems for frequency regulation markets using physics-based models, *Journal of Process Control* 90 (2020) 46–55. doi:10.1016/J.JPROCONT.2020.04.001.
- [47] H. Movahedi, S. Pannala, J. Siegel, S. J. Harris, D. Howey, A. Stefanopoulou, Extra throughput versus days lost in V2G services: Influence of dominant degradation mechanism, *Journal of Energy Storage* 104 (2024) 114242. doi:10.1016/J.EST.2024.114242.
URL <https://linkinghub.elsevier.com/retrieve/pii/S2352152X24038283>
- [48] L. Grüne, J. Pannek, *Nonlinear Model Predictive Control Theory and Algorithms*, 2017. doi:10.1007/978-3-319-46024-6.
URL <http://www.springer.com/series/61>
- [49] E. Prat, R. M. Lusby, J. M. Morales, S. Pineda, P. Pinson, How long is long enough? Finite-horizon approximation of energy storage scheduling problems (11 2024).
URL <http://arxiv.org/abs/2411.17463>

- [50] D. Slaifstein, t. Joel Alpízar-Castillo, t. Alvaro Menendez Agudin, t. Laura Ramírez-Elizondo, G. Ram Chandra Mouli, P. Bauer, Aging-aware Battery Operation for Multicarrier Energy Systems, in: 49th Annual Conference of the IEEE Industrial Electronics Society (IES), Singapore, 2023.
- [51] Home - Elaad NL (2024).
URL <https://platform.elaad.io/>
- [52] B. Planden, K. Lukow, P. Henshall, G. Collier, D. Morrey, A computationally informed realisation algorithm for lithium-ion batteries implemented with LiBRA.jl, *Journal of Energy Storage* 55 (2022) 105637. doi:10.1016/j.est.2022.105637.
URL <https://linkinghub.elsevier.com/retrieve/pii/S2352152X22016255>
- [53] A. Rodríguez, G. L. Plett, M. S. Trimboli, Comparing four model-order reduction techniques, applied to lithium-ion battery-cell internal electrochemical transfer functions, *eTransportation* 1 (2019) 100009. doi:10.1016/j.etrans.2019.100009.
URL <https://linkinghub.elsevier.com/retrieve/pii/S2590116819300098>
- [54] G. Fan, D. Lu, M. S. Trimboli, G. L. Plett, C. Zhu, X. Zhang, Nondestructive diagnostics and quantification of battery aging under different degradation paths, *Journal of Power Sources* 557 (2023) 232555. doi:10.1016/j.jpowsour.2022.232555.
URL <https://linkinghub.elsevier.com/retrieve/pii/S0378775322015324>
- [55] The Green Village, fieldlab voor duurzame innovatie.
URL <https://www.thegreenvillage.org/>
- [56] A. Smets, K. Jäger, O. Isabella, R. van Swaaij, M. Zeman, *Solar Energy: The physics and engineering of photovoltaic conversion, technologies and systems*, UIT Cambridge Ltd, 2016.
URL <https://ebookcentral-proquest-com.tudelft.idm.oclc.org/lib/delft/detail.action?docID=4781743>

- [57] I. Diab, A. Saffirio, G. R. Chandra-Mouli, P. Bauer, A simple method for sizing and estimating the performance of PV systems in trolleybus grids, *Journal of Cleaner Production* 384 (2023) 135623. doi:10.1016/J.JCLEPRO.2022.135623.
- [58] EPEX Spot (2023).
URL <https://www.epexspot.com/en>
- [59] V. Sulzer, S. G. Marquis, R. Timms, M. Robinson, S. J. Chapman, Python battery mathematical modelling (PyBaMM), *Journal of Open Research Software* 9 (1) (2021) 1–8. doi:10.5334/JORS.309.
URL <https://doi.org/10.5334/>
- [60] G. L. Plett, Extended Kalman filtering for battery management systems of LiPB-based HEV battery packs: Part 2. Modeling and identification, *Journal of Power Sources* 134 (2) (2004) 262–276. doi:10.1016/J.JPOWSOUR.2004.02.032.
- [61] J. Bezanson, A. Edelman, S. Karpinski, V. B. Shah, Julia: A Fresh Approach to Numerical Computing, *SIAM Review* 59 (1) (2017) 65–98. doi:10.1137/141000671.
- [62] M. Lubin, O. Dowson, J. D. Garcia, J. Huchette, B. Legat, J. P. Vielma, JuMP 1.0: Recent improvements to a modeling language for mathematical optimization (5 2022).
URL <http://arxiv.org/abs/2206.03866>
- [63] J. L. Pulsipher, W. Zhang, T. J. Hongisto, V. M. Zavala, A unifying modeling abstraction for infinite-dimensional optimization, *Computers & Chemical Engineering* 156 (2022) 107567. doi:10.1016/j.compchemeng.2021.107567.
- [64] R. H. Byrd, J. Nocedal, R. A. Waltz, Knitro: An Integrated Package for Nonlinear Optimization, Springer, Boston, MA, 2006, pp. 35–59. doi:10.1007/0-387-30065-1_{_}4.
URL http://link.springer.com/10.1007/0-387-30065-1_4
- [65] J. Reniers, Degradation-aware optimal control of grid-connected lithium-ion batteries, Ph.D. thesis, University of Oxford (2020).